LOCAL FOURIER ANALYSIS OF MULTIGRID FOR HYBRIDIZED AND EMBEDDED DISCONTINUOUS GALERKIN METHODS[*]

YUNHUI HE[†], SANDER RHEBERGEN[†], AND HANS DE STERCK[†]

Abstract. In this paper we present a geometric multigrid method with Jacobi and Vanka relaxation for hybridized and embedded discontinuous Galerkin discretizations of the Laplacian. We present a local Fourier analysis (LFA) of the two-grid error-propagation operator and show that the multigrid method applied to an embedded discontinuous Galerkin (EDG) discretization is almost as efficient as when applied to a continuous Galerkin discretization. We furthermore show that multigrid applied to an EDG discretization outperforms multigrid applied to a hybridized discontinuous Galerkin (HDG) discretization. Numerical examples verify our LFA predictions.

Key words. Preconditioning, embedded and hybridized discontinuous Galerkin methods, geometric multigrid, local Fourier analysis

AMS subject classifications. 65F08, 65N30, 65N55

1. Introduction. The hybridizable discontinuous Galerkin (HDG) method was introduced in [6] with the purpose of reducing the computational cost of discontinuous Galerkin (DG) methods while retaining the conservation and stability properties of DG methods. This is achieved by introducing facet variables and eliminating local (element-wise) degrees-of-freedom. This static condensation can significantly reduce the size of the global problem. Indeed, it was shown in [21, 37] that the HDG method either outperforms or demonstrates comparable performance when compared to the CG method. This is in part also due to the local postprocessing which allows one to obtain a superconverged solution. However, they mention that these results hold true *only* when a direct solver is used; when an iterative solver is used the HDG method falls behind performance-wise.

The literature on iterative solvers and preconditioners for CG discretizations is vast. In contrast, there are only few studies on solvers for HDG and hybridized discretizations. We mention, for example, [15] which presents a convergence analysis of multigrid for a hybridized Raviart–Thomas discretization, [5] which analyzes an auxiliary space multigrid method for HDG discretizations of elliptic partial differential equations, [10] which considers parallel geometric multigrid for HDG methods, [36] which presents a unified geometric multigrid method for hybridized finite element methods, and [9] which considers the solution of hybridized systems by algebraic multigrid. Furthermore, a performance comparison of a variation of the multigrid method proposed in [5] applied to CG, HDG and DG discretizations for the Poisson problem is conducted in [22]. They show that high-order continuous finite elements give the best time to solution for smooth solutions followed by matrix-free solvers for DG and HDG (using algebraic multigrid).

An alternative to HDG methods is the embedded discontinuous Galerkin (EDG) method which was introduced and analyzed in [7, 16, 34]. The difference between an EDG and HDG method is that the facet variables in an EDG method are continuous between facets; in the HDG method they are discontinuous between facets. For the

---

[†]Department of Applied Mathematics University of Waterloo, 200 University Ave W,Waterloo, ON N2L 3G1, Canada (yunhui.he@uwaterloo.ca, srheberg@uwaterloo.ca, hdesterck@uwaterloo.ca).

EDG method this means that after static condensation it has the same number of global degrees-of-freedom (DOFs) as a continuous Galerkin (CG) method and less DOFs than an HDG method on a given mesh. The EDG method, however, does not have the superconvergent properties of the postprocessed HDG solution and has therefore been studied less in the literature. However, we will see that the algebraic structure of the linear system resulting from an EDG method is better suited to fast iterative solvers than the linear system resulting from an HDG discretization. Indeed, this paper is motivated by the observation that multigrid methods applied to EDG discretizations of the Laplacian outperform multigrid methods applied to HDG discretizations of the Laplacian. This was observed, for example, in the context of the Stokes problem in [25] using the block-preconditioners developed in [24].

The first goal of this paper is to present a geometric multigrid method for the hybridized and embedded discontinuous Galerkin discretizations of the Laplacian. The challenge in designing efficient multigrid methods for these discretizations is twofold. Firstly, since the facet function spaces do not form a nested hierarchy on refined grids, the design of intergrid transfer operators is not trivial. We therefore use the recently introduced Dirichlet-to-Neumann (DtN) maps proposed in [36] for hybridized finite element methods. The second challenge is the design of an efficient relaxation scheme. The smoothers used in multigrid methods applied to discontinuous Galerkin (DG) discretizations of an elliptic PDE are usually the classical (block) Jacobi and (block) Gauss–Seidel smoother (see for example [14, 19, 20, 33]). We, however, use additive Vanka-type relaxation [11, 13, 28] since Vanka-type relaxation is more suitable for parallel computing on general meshes than (block) Gauss–Seidel and, as we will show, results in a multigrid method that requires less iterations than when using Jacobi relaxation. Using Vanka-type relaxation requires the definition of Vanka-patches. We will study two different types of patches, namely, element-wise and vertex-wise patches. We remark that Vanka-type relaxation has been studied also in the context of discontinuous Galerkin methods for the Stokes problem in [1].

The second and main goal of this paper is to present a two-dimensional local Fourier analysis (LFA) of the geometric two-grid error propagation operator of HDG and EDG discretizations of the Laplacian. Local Fourier analysis is used to predict the efficiency of multigrid methods. We will show that the performance of multigrid applied to an embedded discontinuous Galerkin discretization is similarly efficient and scalable to when multigrid is applied to a continuous Galerkin discretization. We furthermore show that multigrid applied to EDG outperforms multigrid applied to HDG, confirming what was previously observed but not explained in [25]. We remark that local Fourier analysis has previously been used to study the performance of multigrid applied to discontinuous Galerkin discretizations (see for example [12, 19, 20, 31, 32, 33]). One-dimensional LFA has been used also to study a multilevel method for the HDG discretization of the Helmholtz equation [4]. However, to the best of our knowledge, a two-dimensional LFA has not been applied in the context of hybridizable and embedded discontinuous Galerkin discretizations, and the performance of geometric multigrid for these types of methods has not been analyzed before.

The remainder of this work is organized as follows. In section 2 we discuss the hybridized and embedded discontinuous Galerkin discretization of the Poisson problem. We present geometric multigrid with additive Vanka relaxation for the hybridized and embedded trace system in section 3. A local Fourier analysis of the corresponding two-grid method is presented in section 4. Our theory is applied and verified by numerical examples in section 5 and we draw conclusions in section 6.

2. The EDG and HDG methods. In this section we present EDG and HDG methods for the Poisson problem:

$$(2.1a) \qquad\qquad -\Delta u = f \qquad\qquad\qquad \text{in } \Omega,$$

$$(2.1b) \qquad\qquad\quad u = 0 \qquad\qquad\qquad\ \text{on } \partial\Omega,$$

where $\Omega \subset \mathbb{R}^2$ is a bounded polygonal domain with boundary $\partial\Omega$, $f : \Omega \to \mathbb{R}$ is a given source term, and $u : \Omega \to \mathbb{R}$ is the unknown.

2.1. The discretization. We will discretize (2.1) by an EDG and an HDG method. For this, denote by $\mathcal{T}_h := \{K\}$ a tesselation of Ω into non-overlapping quadrilateral elements K. We will denote the diameter of an element K by h_K and the maximum diameter over all elements $K \in \mathcal{T}_h$ by h. The boundary of an element is denoted by ∂K and the outward unit normal vector on ∂K is denoted by $\boldsymbol{n}$. An interior face $F := \partial K^+ \cap \partial K^-$ is shared by two adjacent elements K^+ and K^- while a boundary face is a part of ∂K that lies on $\partial\Omega$. We denote the set of all faces by $\mathcal{F}_h := \{F\}$ and the union of all faces by Γ_h^0.

Denote by $Q^k(K)$ and $Q^k(F)$ the spaces of tensor product polynomials of degree k on, respectively, element K and face F. We consider the following discontinuous finite element function spaces:

$$(2.2) \qquad V_h := \left\{ v_h \in L^2(\Omega) \,:\, v_h \in Q^k(K) \,\forall K \in \mathcal{T}_h \right\},$$

$$(2.3) \qquad \bar{V}_h := \left\{ \bar{v}_h \in L^2(\Gamma_h^0) \,:\, \bar{v}_h \in Q^k(F) \,\forall F \in \mathcal{F}_h, \,\bar{v}_h = 0 \text{ on } \partial\Omega \right\}.$$

For the EDG and HDG methods we then define

$$(2.4) \qquad \boldsymbol{X}_h := V_h \times \bar{X}_h \quad \text{with} \quad \bar{X}_h := \begin{cases} \bar{V}_h & \text{HDG method,} \\ \bar{V}_h \cap C^0(\Gamma_h^0) & \text{EDG method.} \end{cases}$$

We note that the HDG method uses discontinuous facet function spaces and that the EDG method uses continuous facet function spaces.

For notational purposes we denote function pairs in $\boldsymbol{X}_h$ by $\boldsymbol{v}_h := (v_h, \bar{v}_h) \in \boldsymbol{X}_h$. For functions $u, v \in L^2(K)$ we write $(u, v)_K := \int_K uv \, dx$ and define $(u, v)_{\mathcal{T}_h} := \sum_{K \in \mathcal{T}_h} (u, v)_K$. Similarly, for functions $u, v \in L^2(E)$ where $E \subset \mathbb{R}$ we write $\langle u, v \rangle_E := \int_E uv \, dx$ and $\langle u, v \rangle_{\partial\mathcal{T}_h} := \sum_{K \in \mathcal{T}_h} \langle u, v \rangle_{\partial K}$.

The interior penalty EDG and HDG methods are given by [6, 7, 34]: find $\boldsymbol{u}_h \in \boldsymbol{X}_h$ such that

$$(2.5) \qquad\qquad a_h(\boldsymbol{u}_h, \boldsymbol{v}_h) = (v_h, f)_{\mathcal{T}_h} \quad \forall \boldsymbol{v}_h \in \boldsymbol{X}_h,$$

where

$$(2.6) \quad a_h(\boldsymbol{w}, \boldsymbol{v}) := (\nabla w, \nabla v)_{\mathcal{T}_h} + \langle \alpha h_K^{-1}(w - \bar{w}), v - \bar{v} \rangle_{\partial\mathcal{T}_h}$$
$$- \langle w - \bar{w}, \nabla v \cdot \boldsymbol{n} \rangle_{\partial\mathcal{T}_h} - \langle v - \bar{v}, \nabla w \cdot \boldsymbol{n} \rangle_{\partial\mathcal{T}_h}.$$

Here α is a penalty parameter that needs to be chosen sufficiently large [34].

2.2. Static condensation. A feature of the EDG and HDG methods is that local (element) degrees-of-freedom can be eliminated from the discretization. For higher-order accurate discretizations this static condensation can significantly reduce the size

of the problem. To obtain the reduced problem we define the function $v_h^L(\bar{m}_h, s) \in V_h$ such that its restriction to the element K satisfies: given $s \in L^2(\Omega)$ and $\bar{m}_h \in \bar{X}_h$,

$$(2.7) \quad (\nabla v_h^L, \nabla w_h)_K + \langle \alpha h_K^{-1} v_h^L, w_h \rangle_{\partial K} - \langle v_h^L, \nabla w_h \cdot \boldsymbol{n} \rangle_{\partial K} - \langle w_h, \nabla v_h^L \cdot \boldsymbol{n} \rangle_{\partial K}$$
$$= (w_h, s)_K + \langle \alpha h_K^{-1} \bar{m}_h, w_h \rangle_{\partial K} - \langle \bar{m}_h, \nabla w_h \cdot \boldsymbol{n} \rangle_{\partial K},$$

for all $w_h \in Q^k(K)$. If $\boldsymbol{u}_h \in \boldsymbol{X}_h$ satisfies (2.5), then $u_h = u_h^f + l(\bar{u}_h)$ where $u_h^f := v_h^L(0, f)$ and $l(\bar{u}_h) := v_h^L(\bar{u}_h, 0)$. Furthermore, $\bar{u}_h \in \bar{X}_h$ satisfies [6, 24]:

$$(2.8) \qquad\qquad \bar{a}_h(\bar{u}_h, \bar{v}_h) = (l(\bar{v}_h), f)_{\mathcal{T}_h} \quad \forall \bar{v}_h \in \bar{X}_h$$

where

$$(2.9) \qquad\qquad \bar{a}_h(\bar{u}_h, \bar{v}_h) := a_h((l(\bar{u}_h), \bar{u}_h), (l(\bar{v}_h), \bar{v}_h)).$$

We remark that (2.8) is the EDG or HDG method after eliminating the element degrees-of-freedom.

It will be useful to consider also the matrix representation of the EDG and HDG methods. For this, let $\mathbf{u}_h \in \mathbb{R}^{n_h}$ be the vector of the discrete solution with respect to the basis for V_h and let $\bar{\mathbf{u}}_h \in \mathbb{R}^{\bar{n}_h}$ be the vector of the discrete solution with respect to the basis for $\bar{V}_h$. We can write (2.5) as

$$(2.10) \qquad\qquad \begin{bmatrix} A & B^T \\ B & C \end{bmatrix} \begin{bmatrix} \mathbf{u}_h \\ \bar{\mathbf{u}}_h \end{bmatrix} = \begin{bmatrix} G_1 \\ G_2 \end{bmatrix},$$

where A, B, C are the matrices obtained from $a_h((0, \cdot), (0, \cdot))$, $a_h((\cdot, 0), (0, \cdot))$, and $a_h((0, \cdot), (0, \cdot))$, respectively. Since A is a block diagonal matrix it is cheap to compute its inverse. Then, using $\mathbf{u}_h = A^{-1}(G_1 - B^T \bar{\mathbf{u}}_h)$ we eliminate $\mathbf{u}_h$ from (2.10) and find:

$$(2.11) \qquad (-BA^{-1}B^T + C)\bar{\mathbf{u}}_h = G_2 - BA^{-1}G_1 \qquad \leftrightarrow \qquad K_h \bar{\mathbf{u}}_h = f_h.$$

This trace system is the matrix representation of (2.8). In the remainder of this work we will present and analyze geometric multigrid with Vanka relaxation for the solution of (2.11).

3. Geometric multigrid method. The geometric multigrid algorithm consists of: (1) applying pre-relaxation on the fine grid; (2) a coarse-grid correction step in which the residual is restricted to a coarse grid, a coarse-grid problem is solved (either exactly or by applying multigrid recursively), interpolating the resulting solution as an error correction to the fine grid approximation; and (3) applying post-relaxation.

In this section we present the different operators in a geometric multigrid method for the solution of the trace system (2.11). To set up notation, let $\mathcal{T}_{n,h}$ be a finite sequence of increasingly coarser meshes with $n = 1, 2, 3, \ldots, N$. For $1 \le n < m \le N$ we denote the restriction operator by $R_{n,h}^{m,h} : \mathcal{T}_{n,h} \to \mathcal{T}_{m,h}$, the prolongation operator by $P_{m,h}^{n,h} : \mathcal{T}_{m,h} \to \mathcal{T}_{n,h}$, and the coarse-grid operator by $K_{m,h}$.

3.1. Relaxation scheme. Many different relaxation methods may be used in multigrid algorithms. In our analysis we consider additive Vanka type relaxation (block Jacobi relaxation defined by Vanka patches) and compare its performance to the classical relaxation iterations of pointwise Jacobi and Gauss–Seidel. In this section we introduce additive Vanka relaxation relaxation [13, 28] following the description in [11].

Let $\mathcal{D}$ denote the set of DOFs of $\bar{\mathbf{u}}_h$ and let $\mathcal{D}_i$, $i = 1, \ldots, J$, be subsets of unknowns with $\mathcal{D} = \cup_{i=1}^{J} \mathcal{D}_i$. Let V_i be the restriction operator mapping from vectors over the set of all unknowns, $\mathcal{D}$, to vectors whose unknowns consist of the DOFs in $\mathcal{D}_i$. Then $K_i = V_i K_h V_i^T$ is the restriction of K_h to the i-th block of DOFs. Moreover, let $W_i = \mathrm{diag}(w_1^i, w_2^i, \ldots, w_{m_i}^i)$ for $i = 1, \ldots, J$ be a diagonal weight matrix for each block i, where m_i is the dimension of K_i. Then, for a given approximation $\bar{\mathbf{u}}_h^{(j)}$, we solve in each Vanka block $i = 1, \ldots, J$ the linear system

$$(3.1) \qquad\qquad K_i \delta_i = V_i(b_h - K_h \bar{\mathbf{u}}_h^{(j)}),$$

and update $\bar{\mathbf{u}}_h^{(j)}$ according to

$$(3.2) \qquad\qquad \bar{\mathbf{u}}_h^{(j+1)} = \bar{\mathbf{u}}_h^{(j)} + \omega \sum_{i=1}^{J} V_i^T W_i \delta_i,$$

where ω is a tunable parameter. For the rest of this paper it is useful to note that the error-propagation operator of the additive Vanka relaxation scheme is given by

$$(3.3) \qquad\qquad S_h = I - \omega M_h^{-1} K_h,$$

where

$$M_h^{-1} = \sum_{i=1}^{J} V_i^T W_i K_i^{-1} V_i.$$

Depending on the discretization method (EDG, HDG, and CG), the sets $\mathcal{D}_i$ $i = 1, \ldots, J$ are chosen differently. However, for all discretization methods we consider two classes of determining $\mathcal{D}_i$, namely, via vertex-wise patches and via element-wise patches. Vertex-wise patches $\mathcal{D}_i$ consist of the DOFs on the vertex $\boldsymbol{v}_i$, the DOFs on the interior of all edges that share vertex $\boldsymbol{v}_i$, and any DOFs on the interiors of the elements that contains vertex $\boldsymbol{v}_i$. On element-wise patches $\mathcal{D}_i$ consists of all DOFs on the ith element and its boundary. As an example we plot the different patches for CG for $k = 2$, EDG for $k = 2$, and HDG for $k = 1$ in Figure 3.1. Note that these two Vanka-type patches are applicable also on unstructured meshes.

Given the set $\mathcal{D}_i$ we next describe the weight matrix $W_i = \mathrm{diag}(w_1^i, \ldots, w_{m_i}^i)$. Here w_k^i is the reciprocal of the number of patches that contain DOF k. For example, consider the case of Continuous Galerkin with $k = 2$ and a vertex-wise Vanka block (see Figure 3.1a). The vertex DOF is not shared by other patches, therefore its weight is 1. The edge degrees-of-freedom are shared by two patches, therefore their weight is 1/2. The DOFs on the interior of an element are shared by four patches, therefore their weight is 1/4. For this example we furthermore note that K_i is a 9×9 matrix and, if K_h is an $n \times n$ matrix, V_i is a $9 \times n$ matrix.

We end this section by noting that the size of K_i increases with increasing degree of the polynomial approximation used in the discretization. To apply the additive Vanka smoother (3.3) it is necessary to compute the inverse of K_i. To reduce the cost of computing K_i^{-1} we therefore also consider a lower-triangular approximation to K_i. We refer to this as Lower-Triangular-Vertex-Wise and Lower-Triangular-Element-Wise Vanka relaxation.
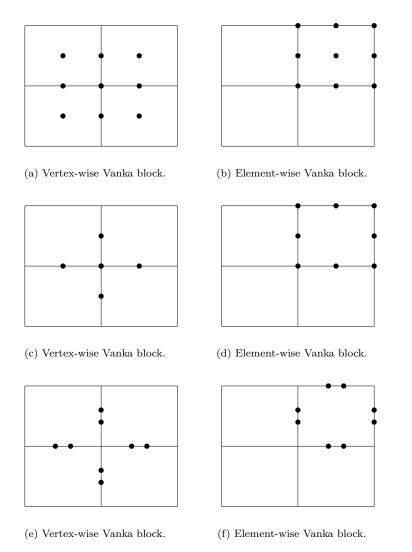
(a) Vertex-wise Vanka block.   (b) Element-wise Vanka block.

(c) Vertex-wise Vanka block.   (d) Element-wise Vanka block.

(e) Vertex-wise Vanka block.   (f) Element-wise Vanka block.

FIG. 3.1. *Vertex- and element-wise Vanka patches. Top row: CG ($k = 2$). Middle row: EDG ($k = 2$). Bottom row: HDG ($k = 1$).*

3.2. Grid-transfer operators and the coarse-grid operator. While standard finite-element interpolation as in [29] can be used for a Continuous Galerkin finite element method, this approach is not possible for hybridized methods since $\bar{X}_{m,h} \not\subseteq \bar{X}_{n,h}$ with $m = n + 1$. We therefore use the Dirichlet-to-Neumann (DtN) interpolation from [36] which we describe next for the HDG and EDG methods.

In what follows, we assume $m = n+1$. First we decompose the set of all fine-level faces in $\mathcal{T}_{n,h}$ as $\mathcal{F}_{n,h} = \mathcal{F}_{n,h}^I \oplus \mathcal{F}_{n,h}^B$, with $\mathcal{F}_{n,h}^B$ the set of all faces in $\mathcal{F}_{n,h}$ that are in the coarse-level face set $\mathcal{F}_{m,h}$ (they form the boundaries of the coarse elements), and with $\mathcal{F}_{n,h}^I$ the set of all faces in $\mathcal{F}_{n,h}$ that are not in $\mathcal{F}_{m,h}$ (they lie in the interior of the coarse elements). The idea is then to split the set of degrees-of-freedom of $\bar{\mathbf{u}}_h$ into two groups $\mathcal{D} = \mathcal{D}_I \cup \mathcal{D}_B$, where $\mathcal{D}_B$ is the set of DOFs located on the edges in $\mathcal{F}_{n,h}^B$ and $\mathcal{D}_I$ is the set of DOFs located on the edges in $\mathcal{F}_{n,h}^I$. We illustrate this for
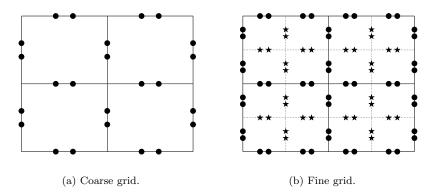
(a) Coarse grid. (b) Fine grid.

FIG. 3.2. *Coarse and fine grids for HDG with $k = 1$. The filled circles are DOFs in $\mathcal{D}_B$ and the stars are DOFs in $\mathcal{D}_I$.*

the HDG method with $k = 1$ on a rectangular mesh in Figure 3.2. Then denoting by $\bar{X}_h^B$ the part of $\bar{X}_h$ corresponding to $\mathcal{D}_B$, it is clear that $\bar{X}_{m,h} \subset \bar{X}_{n,h}^B$.

We adapt [29] to define the first part of the prolongation operator mapping, from $\bar{X}_{m,h}$ to $\bar{X}_{n,h}^B$. In particular, we define $P_B : \bar{X}_{m,h} \rightarrow \bar{X}_{n,h}^B$, with $m = n + 1$, as

$$(3.4) \qquad \sum_{F \in \mathcal{F}_{n,h}^B} \langle P_B \bar{v}, \bar{u} \rangle_F = \sum_{F \in \mathcal{F}_{n,h}^B} \langle \bar{v}, \bar{u} \rangle_F \quad \forall \bar{v} \in \bar{X}_{m,h}, \ \bar{u} \in \bar{X}_{n,h}^B.$$

For the multigrid method, however, we require a prolongation operator $P_{m,h}^{n,h}$ mapping from $\bar{X}_{m,h}$ to the whole of $\bar{X}_{n,h}$, which we discuss next.

Splitting the vector $\bar{\mathbf{u}}_h$ in (2.11) into DOFs in $\mathcal{D}_I$ and $\mathcal{D}_B$ we can write (2.11) as

$$\begin{bmatrix} K_{II} & K_{IB} \\ K_{BI} & K_{BB} \end{bmatrix} \begin{bmatrix} \bar{\mathbf{u}}_I \\ \bar{\mathbf{u}}_B \end{bmatrix} = f_h.$$

We can then define the DtN prolongation operator as

$$(3.5) \qquad P_{m,h}^{n,h} = \begin{bmatrix} P_I \\ P_B \end{bmatrix} = \begin{bmatrix} -K_{II}^{-1} K_{IB} P_B \\ P_B \end{bmatrix}.$$

We remark that this operator can be computed locally. We furthermore remark that it was shown in [36] that this DtN prolongation operator preserves energy when transferring information between two levels, i.e., for $m = n + 1$,

$$\bar{a}_{n,h}(P_{m,h}^{n,h} \bar{v}_{m,h}, P_{m,h}^{n,h} \bar{v}_{m,h}) = \bar{a}_{m,h}(\bar{v}_{m,h}, \bar{v}_{m,h}) \quad \forall \bar{v}_{m,h} \in \bar{X}_{m,h}.$$

Given the prolongation operator we then define the restriction operator as $R_{n,h}^{m,h} = (P_{m,h}^{n,h})^T$ and use the Galerkin approximation of $K_{n,h}$ as our coarse-grid operator, i.e., $K_{m,h} = R_{n,h}^{m,h} K_{n,h} P_{m,h}^{n,h}$.

4. A local Fourier analysis framework for HDG, EDG, and CG. Let $\mathcal{T}_h$ denote a fine mesh of Ω and $\mathcal{T}_H$ denote a coarse mesh of Ω such that $H = 2h$. From now on, all meshes we consider will be Cartesian. The two-grid error-propagation operator is given by

$$(4.1) \qquad E_h = S_h^{\nu_2}(I_h - P_H^h(K_H)^{-1} R_h^H K_h) S_h^{\nu_1},$$

where ν_1, ν_2 are the number of pre- and post relaxation sweeps, respectively, and I_h denotes the identity operator. To analyze the two-grid error-propagation operator, and hence to obtain a measure of the efficiency of the two-grid method applied to HDG, EDG, and CG discretizations of the Poisson problem, we use Local Fourier Analysis (LFA) [30, 35].

LFA was introduced in [3] to study the convergence behavior of multigrid methods for boundary value problems. Assume L_h is a discrete operator obtained by discretizing a PDE on an infinite two dimensional domain. L_h can be thought of as a matrix of infinite size, but we represent it by operators that operate on the DOFs near a generic grid point and that are specified by two-dimensional stencils that we assume have constant stencil coefficients. The eigenfunctions of L_h can be expressed by discrete Fourier modes, resulting in a representation of L_h by an $r \times r$ matrix, $\tilde{L}_h(\boldsymbol{\theta}) \in \mathbb{C}^{r \times r}$ where $\boldsymbol{\theta} \in (-\pi/2, 3\pi/2]^2$ and $r \geq 1$ is small and depends on the discretization. This $\tilde{L}_h(\boldsymbol{\theta})$ is called the symbol of L_h. Specifically, for a scalar PDE, when there is a single degree of freedom located on the mesh of a cartesian grid, then $r = 1$ and the symbol is a scalar. However, when there are different degrees of freedom that may be located at different locations on the grid (e.g. nodes, edges, centers, etc.), then $r > 1$ equals the number of different degrees of freedom, and the symbol is matrix-valued.

Fundamental to LFA is that the properties of L_h can be described by the small matrix $\tilde{L}_h(\boldsymbol{\theta})$. For example, the efficiency of multigrid on a finite grid is measured by the spectral radius of the two-grid error-propagation matrix E_h (4.1). However, since E_h is typically very large, we will find instead the spectral radius of the symbol of the two-grid error-propagation operator corresponding to the extension of E_h to the infinite domain. In contrast to node-based discretization problems with one DOF per node, we consider here discretizations with multiple DOFs per node, edge, and element. The key to LFA is the identification of the eigenspace of K_h and the symbol of K_h, and finding the LFA representation of E_h defined by (4.1). This will be done in this section. The methodology used in our LFA analysis for high-order hybridized and embedded discontinuous Galerkin discretizations of the Laplacian is similar to the methods used in the recent papers [2, 8, 11, 17, 18, 23, 27]. The theory for the invariant space of edge-based operators was first given in [2], for the curl-curl equations. While describing the general principles of the approach in the next sections, we extend the theory of [2] to the case where we have multiple degrees of freedom located on multiple different grid locations, including vertical and horizontal edges, nodes and cell centers of the grid.

4.1. Infinite grid. For our analysis we follow a similar approach as [2] by first defining an appropriate infinite grid and subgrids. To define these subgrids, we first lump all the X-type DOFs on a horizontal edge and Y-type DOFs on a vertical edge to the midpoint of that edge. All C-type DOFs will be lumped to the center of an element and N-type DOFs are located at a node. We then consider the following two-dimensional infinite uniform grid $\boldsymbol{G}_h = \cup_{\alpha \in \{N,X,Y,C\}} \boldsymbol{G}_h^\alpha$, with subgrids

$$(4.2) \qquad \boldsymbol{G}_h^\alpha = \left\{ \boldsymbol{x}^\alpha := (x_1^\alpha, x_2^\alpha) = (k_1, k_2)h + \sigma^\alpha, \ (k_1, k_2) \in \mathbb{Z}^2 \right\},$$

where

$$\sigma^\alpha = \begin{cases} (0,0) & \text{if } \alpha = N, \\ (h/2, 0) & \text{if } \alpha = X, \\ (0, h/2) & \text{if } \alpha = Y, \\ (h/2, h/2) & \text{if } \alpha = C. \end{cases}$$

We will refer to $\boldsymbol{G}_h^N$ as N-type points on the grid $\boldsymbol{G}_h$, associated with N-type DOFs. Furthermore, $\boldsymbol{G}_h^X$, $\boldsymbol{G}_h^Y$, and $\boldsymbol{G}_h^C$ will be referred to as X-, Y-, and C-type points on the grid $\boldsymbol{G}_h$. These are associated, respectively, with X-, Y-, and C-type DOFs. We remark that it is possible that there is more than one DOF at a particular location. We will use subscripts to distinguish between them. For example, X_1 and X_2 are two X-type DOFs on a horizontal edge. The coarse grids $\boldsymbol{G}_H$ are defined similarly.

Remark 4.1. The CG method for $k > 1$ consists of N-, X-, Y-, and C-type DOFs and therefore requires all four subgrids $\boldsymbol{G}_h^\alpha$, $\alpha = N, X, Y, C$. We refer to [18] for the case $k = 2$. For $k = 1$ CG only has N-type DOFs and therefore requires only the $\boldsymbol{G}_h^N$ grid. EDG is identical to CG for $k = 1$. For the EDG method for $k > 1$ the C-type DOFs have been eliminated by static condensation and therefore requires only the subgrids $\boldsymbol{G}_h^\alpha$, $\alpha = N, X, Y$. For $k \geq 1$ the HDG method only has X- and Y-type DOFs and so requires the subgrids $\boldsymbol{G}_h^X$ and $\boldsymbol{G}_h^Y$.

4.2. Partitioning of the discrete operator. Let K_h be the EDG/HDG matrix given by (2.11) or the matrix obtained from a continuous Galerkin discretization of the Laplacian defined on the mesh $\boldsymbol{G}_h$. We will treat K_h as an operator on the infinite mesh $\boldsymbol{G}_h$. To take into account that the DOFs on $\boldsymbol{G}_h^N$, $\boldsymbol{G}_h^X$, $\boldsymbol{G}_h^Y$, and $\boldsymbol{G}_h^C$ are different, we partition the operator K_h according to the different groups of DOFs:

$$(4.3) \qquad K_h = \begin{bmatrix} K_{NN} & K_{NX} & K_{NY} & K_{NC} \\ K_{XN} & K_{XX} & K_{XY} & K_{XC} \\ K_{YN} & K_{YX} & K_{YY} & K_{YC} \\ K_{CN} & K_{CX} & K_{CY} & K_{CC} \end{bmatrix}.$$

When thinking about K_h as an infinite matrix, this corresponds to ordering the grid points in $\boldsymbol{G}_h$ in the order of the subgrids $\boldsymbol{G}_h^\alpha$, $\alpha \in \{N, X, Y, C\}$, and, for example, operator K_{NC} is a mapping from a grid function on C-type points to a grid function on N-type points.

Note furthermore that the EDG method does not include the C-type DOFs and the HDG method does not include the C- and N-type DOFs. As an example, consider the HDG method. Then we write

$$(4.4) \qquad K_h = \begin{bmatrix} K_{XX} & K_{XY} \\ K_{YX} & K_{YY} \end{bmatrix}.$$

If, furthermore, $k = 1$ in HDG (so that there are two DOFs per edge), then we can again partition the submatrix $K_{\alpha\beta}$, $\alpha, \beta \in \{X, Y\}$ into a 2×2-block matrix, which is given by

$$(4.5) \qquad K_{\alpha\beta} = \begin{bmatrix} K_{\alpha_1\beta_1} & K_{\alpha_1\beta_2} \\ K_{\alpha_2\beta_1} & K_{\alpha_2\beta_2} \end{bmatrix},$$

where, for example, the operator $K_{X_1Y_2}$ maps from the second degree of freedom on the Y-edges to the first degree of freedom on the X-edges.

In the general case we use the short-hand notation

$$(4.6) \qquad K_h = (K_{\alpha_i \beta_j}), \quad \text{with} \quad \alpha, \beta \in \{N, X, Y, C\}, \ i = 1, \cdots, r_\alpha, \ j = 1, \cdots, r_\beta,$$

where r_α is the number of DOFs on a single edge (if $\alpha = X$ or $\alpha = Y$), in a single node (if $\alpha = N$), or on a single element (if $\alpha = C$). Let $r = r_N + r_X + r_Y + r_C$ be the total number of DOFs per element.

Let $w_h(\boldsymbol{x})$ be a grid function on $\boldsymbol{G}_h$, and by $w_h(\boldsymbol{x}^\alpha)$ we mean the grid function $w_h(\boldsymbol{x})$ restricted to grid points $\boldsymbol{x}^\alpha \in \boldsymbol{G}_h^\alpha \subset \boldsymbol{G}_h$. Consider operator $K_{\alpha_i \beta_j}$ from the jth degree of freedom on grid $\boldsymbol{G}_h^\beta$ to the ith degree of freedom on grid $\boldsymbol{G}_h^\alpha$. The action of linear operator $K_{\alpha_i \beta_j}$ on grid function $w_h(\boldsymbol{x})$ is given by

$$(4.7) \qquad K_{\alpha_i \beta_j} w_h(\boldsymbol{x}^\alpha) = \sum_{\boldsymbol{\kappa} \in \boldsymbol{V}_{\alpha_i \beta_j}} s_{\boldsymbol{\kappa}}^{(\alpha_i, \beta_j)} w_h(\boldsymbol{x}^\alpha + \boldsymbol{\kappa} h),$$

where the (constant) coefficients $s_{\boldsymbol{\kappa}}^{(\alpha_i, \beta_j)}$ define the stencil representation of $K_{\alpha_i \beta_j}$ as

$$(4.8) \qquad K_{\alpha_i \beta_j} := [s_{\boldsymbol{\kappa}}]_{\alpha_i \beta_j}.$$

Here we assume that only a finite number of coefficients $s_{\boldsymbol{\kappa}}^{(\alpha_i, \beta_j)}$ are nonzero, i.e., $\boldsymbol{V}_{\alpha_i \beta_j}$ is a finite set of offset vectors $\boldsymbol{\kappa}$ such that $\boldsymbol{x}^\alpha + \boldsymbol{\kappa} h \in \boldsymbol{G}_h^\beta$. Note that our notation $K_{\alpha_i \beta_j} w_h(\boldsymbol{x}^\alpha)$ in (4.7) emphasizes that the grid function $K_{\alpha_i \beta_j} w_h$ is defined on grid $\boldsymbol{G}_h^\alpha$, and its function values are linear combinations of values of grid function $w_h(\boldsymbol{x})$ restricted to grid $\boldsymbol{G}_h^\beta$, as expressed in the right-hand side of (4.7).

We now describe the four different possible stencil types for $K_{\alpha_i \beta_j}$. For this, let $\boldsymbol{x} \in \boldsymbol{G}_h^\alpha$ with $\alpha \in \{N, X, Y, C\}$ and denote by $\odot$ a grid point in $\boldsymbol{G}_h^\alpha$ on which the operator acts. Furthermore, let i be a fixed value in $\{1, \ldots, r_\alpha\}$.

Stencil type 1. This considers the case where α_i and β_j in (4.8) share the same grid locations, i.e., $\beta_j = \alpha_j$. Let $\boldsymbol{V}_{\alpha_i \alpha_j}$ be a finite set such that $\boldsymbol{x} + \boldsymbol{\kappa} h \in \boldsymbol{G}_h^\alpha$ for $\kappa \in \boldsymbol{V}_{\alpha_i \alpha_j}$. Then

$$[s_{\boldsymbol{\kappa}}]_{\alpha_i \alpha_j} = \begin{bmatrix} & \vdots & \vdots & \vdots & \\ \cdots & s_{-1,1}^{(\alpha_i, \alpha_j)} & s_{0,1}^{(\alpha_i, \alpha_j)} & s_{1,1}^{(\alpha_i, \alpha_j)} & \cdots \\ & s_{-1,0}^{(\alpha_i, \alpha_j)} & s_{0,0}^{(\alpha_i, \alpha_j)}(\odot) & s_{1,0}^{(\alpha_i, \alpha_j)} & \\ \cdots & s_{-1,-1}^{(\alpha_i, \alpha_j)} & s_{0,-1}^{(\alpha_i, \alpha_j)} & s_{1,-1}^{(\alpha_i, \alpha_j)} & \cdots \\ & \vdots & \vdots & \vdots & \end{bmatrix},$$

where $s_{\kappa_1, \kappa_2}^{(\alpha_i, \alpha_j)} \in \mathbb{R}$ depends on the discretization. Note that $s_{\kappa_1, \kappa_2}^{(\alpha_i, \alpha_j)}$ is the value of the stencil at $\boldsymbol{x} + \boldsymbol{\kappa} h$.

Stencil type 2. Next, let $\boldsymbol{V}_{\alpha_i \beta_j}$ be a finite set such that $\boldsymbol{x} + \boldsymbol{\kappa} h \in \boldsymbol{G}_h^\beta$ with $\kappa \in \boldsymbol{V}_{\alpha_i \beta_j}$ and $\boldsymbol{G}_h^\beta = \{\boldsymbol{y} := \boldsymbol{x} + (h/2, 0), \ \boldsymbol{x} \in \boldsymbol{G}_h^\alpha\}$. Then

$$[s_{\boldsymbol{\kappa}}]_{\alpha_i \beta_j} = \begin{bmatrix} & \vdots & & \vdots & \\ \cdots & s_{-\frac{1}{2},1}^{(\alpha_i, \beta_j)} & & s_{\frac{1}{2},1}^{(\alpha_i, \beta_j)} & \cdots \\ & s_{-\frac{1}{2},0}^{(\alpha_i, \beta_j)} & \odot & s_{\frac{1}{2},0}^{(\alpha_i, \beta_j)} & \\ \cdots & s_{-\frac{1}{2},-1}^{(\alpha_i, \beta_j)} & & s_{\frac{1}{2},-1}^{(\alpha_i, \beta_j)} & \cdots \\ & \vdots & & \vdots & \end{bmatrix}.$$

Stencil type 3. Now let $\boldsymbol{V}_{\alpha_i \beta_j}$ be a finite set such that $\boldsymbol{x} + \boldsymbol{\kappa} h \in \boldsymbol{G}_h^{\beta}$ with $\kappa \in \boldsymbol{V}_{\alpha_i \beta_j}$ and $\boldsymbol{G}_h^{\beta} = \{\boldsymbol{y} := \boldsymbol{x} + (0, h/2), \ \boldsymbol{x} \in \boldsymbol{G}_h^{\alpha}\}$. Then

$$[s_{\boldsymbol{\kappa}}]_{\alpha_i \beta_j} = \begin{bmatrix} & \vdots & \vdots & \vdots & \\ \cdots & s_{-1,\frac{1}{2}}^{(\alpha_i, \beta_j)} & s_{0,\frac{1}{2}}^{(\alpha_i, \beta_j)} & s_{1,\frac{1}{2}}^{(\alpha_i, \beta_j)} & \cdots \\ & & \odot & & \\ \cdots & s_{-1,-\frac{1}{2}}^{(\alpha_i, \beta_j)} & s_{0,-\frac{1}{2}}^{(\alpha_i, \beta_j)} & s_{1,-\frac{1}{2}}^{(\alpha_i, \beta_j)} & \cdots \\ & \vdots & \vdots & \vdots & \end{bmatrix}.$$

Stencil type 4. Finally, let $\boldsymbol{V}_{\alpha_i \beta_j}$ be a finite set such that $\boldsymbol{x} + \boldsymbol{\kappa} h \in \boldsymbol{G}_h^{\beta}$ with $\kappa \in \boldsymbol{V}_{\alpha_i \beta_j}$ and $\boldsymbol{G}_h^{\beta} = \{\boldsymbol{y} := \boldsymbol{x} + (h/2, h/2), \ \boldsymbol{x} \in \boldsymbol{G}_h^{\alpha}\}$. Then

$$[s_{\boldsymbol{\kappa}}]_{\alpha_i \beta_j} = \begin{bmatrix} & \vdots & & \vdots & \\ \cdots & s_{-\frac{1}{2},\frac{1}{2}}^{(\alpha_i, \beta_j)} & & s_{\frac{1}{2},\frac{1}{2}}^{(\alpha_i, \beta_j)} & \cdots \\ & & \odot & & \\ \cdots & s_{-\frac{1}{2},-\frac{1}{2}}^{(\alpha_i, \beta_j)} & & s_{\frac{1}{2},-\frac{1}{2}}^{(\alpha_i, \beta_j)} & \cdots \\ & \vdots & & \vdots & \end{bmatrix}.$$

We remark that not all stencil types are used for all discretizations. For example, the HDG method only uses stencil types 1 and 4, and EDG and CG use all 4 stencil types. We present an example of the stencil notation (4.8) for the HDG method with $k = 1$ in Appendix A.

4.3. Properties of the symbol of K_h. In this section we will determine the symbol of K_h. Note that K_h is a block operator with r^2 blocks that are each characterized by a stencil as defined in (4.7) and (4.8). We will follow a similar approach as presented in [2] to account for K_h acting on different groups of DOFs, see Eq. (4.3). Our aim is to characterize the eigenfunctions of K_h in terms of the Fourier modes

$$(4.9) \qquad \varphi_h(\boldsymbol{\theta}; \boldsymbol{x}) = e^{\iota \boldsymbol{\theta} \cdot \boldsymbol{x}/h},$$

where $\iota^2 = -1$. Each of the operators $K_{\alpha_i \beta_j}$ is a block Toeplitz operator with Toeplitz blocks, and as such their eigenfunctions are given by (4.9), but we need to determine how these eigenfunctions combine to make up invariant subspaces of K_h, taking into account the different degrees of freedom and the different grid locations. To account for this we redefine the grid.

Let $\alpha \in \{N, X, Y, C\}$ and let there be r_α DOFs, denoted by $\alpha_1, \ldots, \alpha_{r_\alpha}$, located at location α. We define r_α copies of $\boldsymbol{G}_h^{\alpha}$, i.e., $\boldsymbol{G}_h^{\alpha_1} = \ldots = \boldsymbol{G}_h^{\alpha_{r_\alpha}} = \boldsymbol{G}_h^{\alpha}$. We then define the 'extended' grid $\widetilde{\boldsymbol{G}}_h$ in which we order the grid points as follows: all grid points in $\boldsymbol{G}_h^{N_1}$ followed by the grid points in $\boldsymbol{G}_h^{N_2}, \ldots, \boldsymbol{G}_h^{N_{r_N}}$, then the r_X copies of the grid points in $\boldsymbol{G}_h^{X}$, the r_Y copies of the grid points in $\boldsymbol{G}_h^{Y}$, and the r_C copies of the grid points in $\boldsymbol{G}_h^{C}$ (note that this ordering is consistent with the ordering of $K_{\alpha_i \beta_j}$ in (4.6)). We denote the definition of the extended grid using the $\bigotimes$ symbol:

$$(4.10) \qquad \widetilde{\boldsymbol{G}}_h = \bigotimes_{\alpha \in \{N, X, Y, C\}, i \in \{1, 2, \cdots, r_\alpha\}} \boldsymbol{G}_h^{\alpha_i}.$$

We note that $\widetilde{\boldsymbol{G}}_H$ is defined similarly.

For example, for HDG with $k = 1$ we write

$$(4.11) \qquad \widetilde{\boldsymbol{G}}_h = \boldsymbol{G}_h^{X_1} \bigotimes \boldsymbol{G}_h^{X_2} \bigotimes \boldsymbol{G}_h^{Y_1} \bigotimes \boldsymbol{G}_h^{Y_2}.$$

Consider now the application of the discrete operator K_h acting on a function $w_h(\boldsymbol{x})$ defined on $\widetilde{\boldsymbol{G}}_h$. Considering the restriction of the grid function $K_h w_h(\boldsymbol{x})$ to the α_i grid, i.e., evaluating $K_h w_h(\boldsymbol{x})$ in $\boldsymbol{x}^{\alpha_i} \in \boldsymbol{G}_h^{\alpha_i}$, we obtain

$$(4.12) \qquad K_h w_h(\boldsymbol{x}^{\alpha_i}) = \sum_{\beta \in \{N,X,Y,C\}} \sum_{j=1}^{r_\beta} K_{\alpha_i \beta_j} w_h(\boldsymbol{x}^{\alpha_i})$$

$$(4.13) \qquad = \sum_{\beta \in \{N,X,Y,C\}} \sum_{j=1}^{r_\beta} \sum_{\boldsymbol{\kappa} \in \boldsymbol{V}_{\alpha_i \beta_j}} s_{\boldsymbol{\kappa}}^{(\alpha_i,\beta_j)} w_h(\boldsymbol{x}^{\alpha_i} + \boldsymbol{\kappa} h).$$

Note that, in (4.13), the grid function $w_h(\boldsymbol{x})$ is evaluated on the β_j grid, with $\boldsymbol{\kappa} \in \boldsymbol{V}_{\alpha_i \beta_j}$ and $\boldsymbol{x}^{\alpha_i} + \boldsymbol{\kappa} h \in \boldsymbol{G}_h^{\beta_j}$.

In particular, if we take $w_h(\boldsymbol{x})$ to be the Fourier mode $\varphi_h(\boldsymbol{\theta}; \boldsymbol{x})$ from (4.9) defined on all grid points $\boldsymbol{x} \in \widetilde{\boldsymbol{G}}_h$, we obtain, for the grid function $K_h \varphi_h(\boldsymbol{\theta}; \boldsymbol{x})$ evaluated on the α_i grid, i.e., in $\boldsymbol{x}^{\alpha_i} \in \boldsymbol{G}_h^{\alpha_i}$,

$$K_h \varphi_h(\boldsymbol{\theta}; \boldsymbol{x}^{\alpha_i}) = \sum_{\beta \in \{N,X,Y,C\}} \sum_{j=1}^{r_\beta} K_{\alpha_i \beta_j} \varphi_h(\boldsymbol{\theta}; \boldsymbol{x}^{\alpha_i})$$

$$= \sum_{\beta \in \{N,X,Y,C\}} \sum_{j=1}^{r_\beta} \sum_{\boldsymbol{\kappa} \in \boldsymbol{V}_{\alpha_i \beta_j}} s_{\boldsymbol{\kappa}}^{(\alpha_i,\beta_j)} \varphi_h(\boldsymbol{\theta}; \boldsymbol{x}^{\alpha_i} + \boldsymbol{\kappa} h)$$

$$(4.14) \qquad = \sum_{\beta \in \{N,X,Y,C\}} \sum_{j=1}^{r_\beta} \sum_{\boldsymbol{\kappa} \in \boldsymbol{V}_{\alpha_i \beta_j}} s_{\boldsymbol{\kappa}}^{(\alpha_i,\beta_j)} e^{\iota \boldsymbol{\theta} \cdot \boldsymbol{\kappa}} \varphi_h(\boldsymbol{\theta}; \boldsymbol{x}^{\alpha_i})$$

$$= \sum_{\beta \in \{N,X,Y,C\}} \sum_{j=1}^{r_\beta} \widetilde{K}_{\alpha_i \beta_j}(\boldsymbol{\theta}) \varphi_h(\boldsymbol{\theta}; \boldsymbol{x}^{\alpha_i}),$$

where we define

$$(4.15) \qquad \widetilde{K}_{\alpha_i \beta_j}(\boldsymbol{\theta}) := \sum_{\boldsymbol{\kappa} \in \boldsymbol{V}_{\alpha_i \beta_j}} s_{\boldsymbol{\kappa}}^{(\alpha_i,\beta_j)} e^{\iota \boldsymbol{\theta} \cdot \boldsymbol{\kappa}}.$$

The scalar $\widetilde{K}_{\alpha_i \beta_j}(\boldsymbol{\theta})$ in (4.15) is called the symbol of the operator block $K_{\alpha_i \beta_j}$, taking into account the offset between the grids for DOF α_i and DOF β_j as encoded in the $\boldsymbol{\kappa} \in \boldsymbol{V}_{\alpha_i \beta_j}$.

Let us now define $r = r_N + r_X + r_Y + r_C$ grid functions $\Psi_j^\alpha(\boldsymbol{\theta}; \boldsymbol{x})$ on the grid $\widetilde{\boldsymbol{G}}_h$ by

$$(4.16) \qquad \Psi_j^\alpha(\boldsymbol{\theta}; \boldsymbol{x}) := \begin{cases} \varphi_h(\boldsymbol{\theta}; \boldsymbol{x}) & \text{on the } \alpha_j \text{ grid, i.e., when } \boldsymbol{x} \in \boldsymbol{G}_h^{\alpha_j}, \\ 0 & \text{on all other grids,} \end{cases}$$

and the r-dimensional function space

$$(4.17) \quad \mathcal{F}_h(\boldsymbol{\theta}) = \text{span}\big\{ \Psi_1^N(\boldsymbol{\theta}; \cdot), \dots, \Psi_{r_N}^N(\boldsymbol{\theta}; \cdot), \Psi_1^X(\boldsymbol{\theta}; \cdot), \dots, \Psi_{r_X}^X(\boldsymbol{\theta}; \cdot),$$
$$\Psi_1^Y(\boldsymbol{\theta}; \cdot), \dots, \Psi_{r_Y}^Y(\boldsymbol{\theta}; \cdot), \Psi_1^C(\boldsymbol{\theta}; \cdot), \dots, \Psi_{r_C}^C(\boldsymbol{\theta}; \cdot) \big\}.$$

We will prove, see Theorem 4.2, that $\mathcal{F}_h(\boldsymbol{\theta})$ is an *invariant* function space for the operator K_h.

This result is key to LFA, since LFA depends on computing error reduction factors for different frequencies $\boldsymbol{\theta}$. Due to the invariant function space property for a fixed value of $\boldsymbol{\theta}$, this error reduction factor can be computed for each value of $\boldsymbol{\theta}$ separately. We remark that $\mathcal{F}_h(\boldsymbol{\theta})$ is an extension of the invariant space for edge-based operators introduced in [2]. We require the following definitions and notation.

Let $\widehat{\Psi}^\alpha = [\Psi_1^\alpha, \cdots, \Psi_{r_\alpha}^\alpha]$, $\alpha \in \{N, X, Y, C\}$ and

$$(4.18) \qquad \boldsymbol{\Psi} = \begin{bmatrix} \widehat{\Psi}^N & \widehat{\Psi}^X & \widehat{\Psi}^Y & \widehat{\Psi}^C \end{bmatrix},$$

and note that any function $\Phi(\boldsymbol{\theta}; \cdot) \in \mathcal{F}_h(\boldsymbol{\theta})$ is a linear combination of the basis functions $\Psi_j^\alpha(\boldsymbol{\theta}; \cdot)$:

$$(4.19) \qquad \Phi(\boldsymbol{\theta}; \cdot) = \sum_{\alpha \in \{N,X,Y,C\}} \sum_{j=1,\cdots,r_\alpha} \xi_j^\alpha \Psi_j^\alpha(\boldsymbol{\theta}; \cdot), \qquad \xi_j^\alpha \in \mathbb{C}.$$

Alternatively, we can write

$$\Phi(\boldsymbol{\theta}; \cdot) = \boldsymbol{\Psi}\boldsymbol{\xi}, \quad \text{where} \quad \boldsymbol{\xi} = \begin{bmatrix} \xi^N \\ \xi^X \\ \xi^Y \\ \xi^C \end{bmatrix}, \quad \xi^\alpha = \begin{bmatrix} \xi_1^\alpha \\ \xi_2^\alpha \\ \vdots \\ \xi_{r_\alpha}^\alpha \end{bmatrix}, \quad \alpha \in \{N, X, Y, C\}.$$

We now show that $\mathcal{F}_h(\boldsymbol{\theta})$ is an invariant function space for the operator K_h.

THEOREM 4.2. *For any $\boldsymbol{\theta}$ in $\mathbb{R}^2$ and $\Phi(\boldsymbol{\theta}; \cdot) \in \mathcal{F}_h(\boldsymbol{\theta})$ it holds that*

$$(4.20) \qquad K_h\Phi(\boldsymbol{\theta}; \cdot) = K_h\boldsymbol{\Psi}\boldsymbol{\xi} = \boldsymbol{\Psi}\widetilde{K}_h\boldsymbol{\xi} \in \mathcal{F}_h(\boldsymbol{\theta}),$$

where the $r \times r$ complex matrix

$$\widetilde{K}_h = (\widetilde{K}_{\alpha_i\beta_j})$$

is called the symbol of the operator K_h.

Proof. By (4.19),

$$(4.21) \qquad \begin{aligned} K_h\Phi(\boldsymbol{\theta}; \boldsymbol{x}) &= K_h\left(\sum_{\beta \in \{N,X,Y,C\}} \sum_{j=1,\cdots,r_\beta} \xi_j^\beta \Psi_j^\beta(\boldsymbol{\theta}; \boldsymbol{x})\right) \\ &= \sum_{\beta \in \{N,X,Y,C\}} \sum_{j=1,\cdots,r_\beta} \xi_j^\beta K_h\Psi_j^\beta(\boldsymbol{\theta}; \boldsymbol{x}). \end{aligned}$$

Considering the restriction of the grid function $K_h\Phi(\boldsymbol{\theta}; \boldsymbol{x})$ to the α_i grid, i.e., evalu-

ating $K_h\Phi(\boldsymbol{\theta};\boldsymbol{x})$ in $\boldsymbol{x}^{\alpha_i}\in\boldsymbol{G}_h^{\alpha_i}$, we obtain, using (4.12), (4.13) and (4.14),

$$
\begin{aligned}
K_h\Psi_j^\beta(\boldsymbol{\theta};\boldsymbol{x}^{\alpha_i}) &= \sum_{\gamma\in\{N,X,Y,C\}}\sum_{k=1}^{r_\gamma}\left(K_{\alpha_i\gamma_k}\Psi_j^\beta(\boldsymbol{\theta};\boldsymbol{x}^{\alpha_i})\right) \\
&= \sum_{\gamma\in\{N,X,Y,C\}}\sum_{k=1}^{r_\gamma}\Big(\sum_{\boldsymbol{\kappa}\in\boldsymbol{V}_{\alpha_i\beta_j}}s_{\boldsymbol{\kappa}}^{(\alpha_i,\gamma_k)}\Psi_j^\beta(\boldsymbol{\theta};\boldsymbol{x}^{\alpha_i}+\boldsymbol{\kappa}h)\Big) \\
&= \sum_{\boldsymbol{\kappa}}s_{\boldsymbol{\kappa}}^{(\alpha_i,\beta_j)}\varphi_h(\boldsymbol{\theta};\boldsymbol{x}^{\alpha_i}+\boldsymbol{\kappa}h) \\
&= \sum_{\boldsymbol{\kappa}\in\boldsymbol{V}_{\alpha_i\beta_j}}s_{\boldsymbol{\kappa}}^{(\alpha_i,\beta_j)}e^{\iota\boldsymbol{\theta}\cdot\boldsymbol{\kappa}}\varphi_h(\boldsymbol{\theta};\boldsymbol{x}^{\alpha_i}) \\
&= \widetilde{K}_{\alpha_i\beta_j}\varphi_h(\boldsymbol{\theta};\boldsymbol{x}^{\alpha_i}) \\
&= \widetilde{K}_{\alpha_i\beta_j}\Psi_i^\alpha(\boldsymbol{\theta};\boldsymbol{x}^{\alpha_i}).
\end{aligned}
$$

It then follows from (4.21), on grid α_i, that

$$
(4.22)\qquad K_h\Phi(\boldsymbol{\theta};\boldsymbol{x}^{\alpha_i}) = \sum_{\beta\in\{N,X,Y,C\}}\sum_{j=1,\cdots,r_\beta}\xi_j^\beta\widetilde{K}_{\alpha_i\beta_j}\Psi_i^\alpha(\boldsymbol{\theta};\boldsymbol{x}^{\alpha_i}).
$$

Since $\alpha\in\{N,X,Y,C\}$ and $i\in\{1,2,\cdots,r_\alpha\}$ are arbitrary, (4.22) implies (4.20) as follows. Considering $K_h\Phi(\boldsymbol{\theta};\boldsymbol{x})$ for a generic $\boldsymbol{x}\in\widetilde{\boldsymbol{G}}_h$ on any of the r subgrids, we can sum the right hand side of (4.22) over all grids to obtain

$$
\begin{aligned}
K_h\Phi(\boldsymbol{\theta};\boldsymbol{x}) &= \sum_{\alpha\in\{N,X,Y,C\}}\sum_{i=1,\cdots,r_\alpha}\Psi_i^\alpha(\boldsymbol{\theta};\boldsymbol{x})\sum_{\beta\in\{N,X,Y,C\}}\sum_{j=1,\cdots,r_\beta}\xi_j^\beta\widetilde{K}_{\alpha_i\beta_j} \\
&= \boldsymbol{\Psi}\widetilde{K}_h\boldsymbol{\xi},
\end{aligned}
$$

using the fact that the $\Psi_i^\alpha(\boldsymbol{\theta};\boldsymbol{x})$ have zero overlap in the sum due to (4.16). $\qquad\square$

We now consider frequency aliasing and generalize [2, Theorem 3.2].

THEOREM 4.3. *Let* $\boldsymbol{\eta}=(\eta_1,\eta_2)\in\{(0,0),(1,0),(0,1),(1,1)\}$. *For any* $\boldsymbol{\theta}\in\mathbb{R}^2$, $\boldsymbol{x}\in\widetilde{\boldsymbol{G}}_h$, *and* $\Phi(\boldsymbol{\theta};\boldsymbol{x})$ *in* $\mathcal{F}_h(\boldsymbol{\theta})$, *we have that*

$$
(4.23)\qquad \Phi(\boldsymbol{\theta}+2\pi\boldsymbol{\eta};\boldsymbol{x}) = \Phi(\boldsymbol{\theta};\boldsymbol{x})\times
\begin{cases}
1 & \text{if } \boldsymbol{x}\in\bigotimes_{i\in\{1,\cdots,r_N\}}\boldsymbol{G}_h^{N_i}, \\
(-1)^{\eta_1} & \text{if } \boldsymbol{x}\in\bigotimes_{i\in\{1,\cdots,r_X\}}\boldsymbol{G}_h^{X_i}, \\
(-1)^{\eta_2} & \text{if } \boldsymbol{x}\in\bigotimes_{i\in\{1,\cdots,r_Y\}}\boldsymbol{G}_h^{Y_i}, \\
(-1)^{\eta_1+\eta_2} & \text{if } \boldsymbol{x}\in\bigotimes_{i\in\{1,\cdots,r_C\}}\boldsymbol{G}_h^{C_i}.
\end{cases}
$$

Proof. By (4.19) and (4.16) we need to verify that

$$
(4.24a)\qquad \varphi_h(\boldsymbol{\theta}+2\pi\boldsymbol{\eta};\boldsymbol{x}) = \varphi_h(\boldsymbol{\theta};\boldsymbol{x}),\qquad\qquad \text{if }\ \boldsymbol{x}\in\bigotimes_{i=1,\cdots,r_N}\boldsymbol{G}_h^{N_i},
$$

$$
(4.24b)\qquad \varphi_h(\boldsymbol{\theta}+2\pi\boldsymbol{\eta};\boldsymbol{x}) = (-1)^{\eta_1}\varphi_h(\boldsymbol{\theta};\boldsymbol{x}),\qquad\qquad \text{if }\ \boldsymbol{x}\in\bigotimes_{i=1,\cdots,r_X}\boldsymbol{G}_h^{X_i},
$$

$$
(4.24c)\qquad \varphi_h(\boldsymbol{\theta}+2\pi\boldsymbol{\eta};\boldsymbol{x}) = (-1)^{\eta_2}\varphi_h(\boldsymbol{\theta};\boldsymbol{x}),\qquad\qquad \text{if }\ \boldsymbol{x}\in\bigotimes_{i=1,\cdots,r_Y}\boldsymbol{G}_h^{Y_i},
$$

$$
(4.24d)\qquad \varphi_h(\boldsymbol{\theta}+2\pi\boldsymbol{\eta};\boldsymbol{x}) = (-1)^{\eta_1+\eta_2}\varphi_h(\boldsymbol{\theta};\boldsymbol{x}),\qquad\qquad \text{if }\ \boldsymbol{x}\in\bigotimes_{i=1,\cdots,r_C}\boldsymbol{G}_h^{C_i}.
$$

We show (4.24a). If $\boldsymbol{x} \in \boldsymbol{G}_h^N$ then $\boldsymbol{x} = (ih, jh)$ with $i, j \in \mathbb{Z}$. Then

$$\varphi_h(\boldsymbol{\theta} + 2\pi\boldsymbol{\eta}; \boldsymbol{x}) = e^{\iota(\theta_1 + 2\pi\eta_1)i}e^{\iota(\theta_2 + 2\pi\eta_2)j} = \varphi_h(\boldsymbol{\theta}; \boldsymbol{x})e^{\iota 2\pi\eta_1 i}e^{\iota 2\pi\eta_2 j} = \varphi_h(\boldsymbol{\theta}; \boldsymbol{x}).$$

Equations (4.24b)–(4.24d) follow similarly. □

Due to the frequency aliasing as shown by Theorem 4.3, it is sufficient to consider $\boldsymbol{\theta} = (\theta_1, \theta_2) \in [-\pi/2, 3\pi/2)^2$ (or any pair of intervals with length 2π) in the LFA analysis of our multigrid methods.

4.4. Two-grid LFA. We now determine the symbol of the two-grid error propagation operator (4.1). In order to apply LFA to the two-grid error propagation operator we need to determine how the operators K_h, P_H^h, R_h^H, S_h, and K_H act on the Fourier components $\Phi(\boldsymbol{\theta}; \cdot)$ in $\mathcal{F}_h(\boldsymbol{\theta})$. Note that the Fourier modes on the coarse grid $\widetilde{\boldsymbol{G}}_H$ are given by

$$(4.25) \qquad \Phi_H(\boldsymbol{\theta}; \cdot) = \sum_{\alpha \in \{N, X, Y, C\}} \sum_{j=1, \cdots, r_\alpha} \xi_j^\alpha \bar{\Psi}_j^\alpha(\boldsymbol{\theta}; \cdot),$$

where

$$(4.26) \qquad \bar{\Psi}_j^\alpha(\boldsymbol{\theta}; \boldsymbol{x}) = \begin{cases} \varphi_H(\boldsymbol{\theta}; \boldsymbol{x}) & \text{if } \boldsymbol{x} \in \boldsymbol{G}_H^{\alpha_j}, \\ 0 & \text{otherwise.} \end{cases}$$

We have the following properties of Fourier modes on $\widehat{\boldsymbol{G}}_H$.

THEOREM 4.4. *Let $\boldsymbol{\eta} = (\eta_1, \eta_2) \in \{(0,0), (1,0), (0,1), (1,1)\}$. For any $\boldsymbol{\theta} \in \mathbb{R}^2$, $\boldsymbol{x} \in \widehat{\boldsymbol{G}}_H$, and $\Phi(\boldsymbol{\theta}; \boldsymbol{x})$ in $\mathcal{F}_h(\boldsymbol{\theta})$, we have that*

$$(4.27) \qquad \Phi(\boldsymbol{\theta} + \pi\boldsymbol{\eta}; \boldsymbol{x}) = \Phi(\boldsymbol{\theta}; \boldsymbol{x}) \times \begin{cases} 1 & \text{if } \boldsymbol{x} \in \bigotimes_{i \in \{1, \cdots, r_N\}} \boldsymbol{G}_H^{N_i}, \\ (-1)^{\eta_1} & \text{if } \boldsymbol{x} \in \bigotimes_{i \in \{1, \cdots, r_X\}} \boldsymbol{G}_H^{X_i}, \\ (-1)^{\eta_2} & \text{if } \boldsymbol{x} \in \bigotimes_{i \in \{1, \cdots, r_Y\}} \boldsymbol{G}_H^{Y_i}, \\ (-1)^{\eta_1 + \eta_2} & \text{if } \boldsymbol{x} \in \bigotimes_{i \in \{1, \cdots, r_C\}} \boldsymbol{G}_H^{C_i}. \end{cases}$$

Furthermore, for $\boldsymbol{x} \in \widehat{\boldsymbol{G}}_H$ and $\boldsymbol{\theta} \in [-\pi/2, \pi/2)^2$ we have

$$(4.28) \qquad \Phi(\boldsymbol{\theta} + \pi\boldsymbol{\eta}; \boldsymbol{x}) = \Phi_H(2\boldsymbol{\theta}; \boldsymbol{x}) \times \begin{cases} 1 & \text{if } \boldsymbol{x} \in \bigotimes_{i \in \{1, \cdots, r_N\}} \boldsymbol{G}_H^{N_i}, \\ (-1)^{\eta_1} & \text{if } \boldsymbol{x} \in \bigotimes_{i \in \{1, \cdots, r_X\}} \boldsymbol{G}_H^{X_i}, \\ (-1)^{\eta_2} & \text{if } \boldsymbol{x} \in \bigotimes_{i \in \{1, \cdots, r_Y\}} \boldsymbol{G}_H^{Y_i}, \\ (-1)^{\eta_1 + \eta_2} & \text{if } \boldsymbol{x} \in \bigotimes_{i \in \{1, \cdots, r_C\}} \boldsymbol{G}_H^{C_i}. \end{cases}$$

Proof. We omit the proof since it is similar to the proof of Theorem 4.3. □

We denote the high and low frequency intervals as

$$T^{\text{low}} = [-\tfrac{\pi}{2}, \tfrac{\pi}{2})^2, \qquad T^{\text{high}} = [-\tfrac{\pi}{2}, \tfrac{3\pi}{2})^2 \backslash [-\tfrac{\pi}{2}, \tfrac{\pi}{2})^2.$$

Aliasing of modes will occur in the intergrid transfer operations (see [30, 35]). For this reason we introduce the $4r$-dimensional harmonic space $\mathfrak{F}_h(\boldsymbol{\theta})$, with $\boldsymbol{\theta} \in T^{\text{low}}$, as

$$\mathfrak{F}_h(\boldsymbol{\theta}) = \text{span} \left\{ \boldsymbol{\psi}(\boldsymbol{\theta}^{(\boldsymbol{\eta})}; \cdot) : \boldsymbol{\psi} \in \mathcal{F}_h(\boldsymbol{\theta}), \boldsymbol{\eta} = (\eta_1, \eta_2) \in \{(0,0), (1,0), (0,1), (1,1)\} \right\},$$

where $\boldsymbol{\theta}^{(\boldsymbol{\eta})} = \boldsymbol{\theta}^{(\eta_1,\eta_2)} := (\theta_1 + \pi\eta_1, \theta_2 + \pi\eta_2) = \boldsymbol{\theta} + \pi\boldsymbol{\eta}$ and $\boldsymbol{\theta} = \boldsymbol{\theta}^{(0,0)} \in T^{\text{low}}$. Note that every function $\boldsymbol{\psi} \in \mathfrak{F}_h(\boldsymbol{\theta})$ can be written as follows, using the $\boldsymbol{\Psi}$ matrix defined in (4.18):

$$(4.29) \quad \boldsymbol{\psi} = \boldsymbol{\Psi}(\boldsymbol{\theta}^{(0,0)};\cdot)\,\boldsymbol{\xi}^{(0,0)} + \boldsymbol{\Psi}(\boldsymbol{\theta}^{(1,0)};\cdot)\,\boldsymbol{\xi}^{(1,0)} + \boldsymbol{\Psi}(\boldsymbol{\theta}^{(0,1)};\cdot)\,\boldsymbol{\xi}^{(0,1)} + \boldsymbol{\Psi}(\boldsymbol{\theta}^{(1,1)};\cdot)\,\boldsymbol{\xi}^{(1,1)},$$

where the $\boldsymbol{\xi}^{\boldsymbol{\eta}} \in \mathbb{C}^{r\times 1}$ are uniquely determined.

We remark that $\mathfrak{F}_h(\boldsymbol{\theta})$ is invariant for the two-grid error operator (we refer to [30, Section 4.4] for a discussion on how to prove this for node-based problems), i.e., for any $\boldsymbol{\psi}$ in (4.29),

$$E_h\boldsymbol{\psi} = E_h \left[\boldsymbol{\Psi}(\boldsymbol{\theta}^{(0,0)};\cdot)\ \boldsymbol{\Psi}(\boldsymbol{\theta}^{(1,0)};\cdot)\ \boldsymbol{\Psi}(\boldsymbol{\theta}^{(0,1)};\cdot)\ \boldsymbol{\Psi}(\boldsymbol{\theta}^{(1,1)};\cdot) \right] \widehat{\boldsymbol{\xi}}$$
$$= \left[\boldsymbol{\Psi}(\boldsymbol{\theta}^{(0,0)};\cdot)\ \boldsymbol{\Psi}(\boldsymbol{\theta}^{(1,0)};\cdot)\ \boldsymbol{\Psi}(\boldsymbol{\theta}^{(0,1)};\cdot)\ \boldsymbol{\Psi}(\boldsymbol{\theta}^{(1,1)};\cdot) \right] \widetilde{\boldsymbol{E}}_h\widehat{\boldsymbol{\xi}},$$

where $\widehat{\boldsymbol{\xi}} = [\boldsymbol{\xi}^{(0,0)}\ \boldsymbol{\xi}^{(1,0)}\ \boldsymbol{\xi}^{(0,1)}\ \boldsymbol{\xi}^{(0,0)}]^T \in \mathbb{C}^{4r\times 1}$, and $\widetilde{\boldsymbol{E}}_h$ is the $4r \times 4r$ matrix which is the LFA representation of the two-grid operator E_h given by

$$(4.30) \qquad \widetilde{\boldsymbol{E}}_h(\boldsymbol{\theta},\omega) = \widetilde{\boldsymbol{S}}_h^{\nu_2}(\boldsymbol{\theta},\omega) \left(I - \widetilde{\boldsymbol{P}}_H^h(\boldsymbol{\theta})(\widetilde{K}_H(2\boldsymbol{\theta}))^{-1}\widetilde{\boldsymbol{R}}_h^H(\boldsymbol{\theta})\widetilde{\boldsymbol{\mathcal{K}}}_h(\boldsymbol{\theta}) \right) \widetilde{\boldsymbol{S}}_h^{\nu_1}(\boldsymbol{\theta},\omega),$$

where

$$\widetilde{\boldsymbol{\mathcal{K}}}_h(\boldsymbol{\theta}) = \text{diag}\left\{ \widetilde{K}_h(\boldsymbol{\theta}^{(0,0)}), \widetilde{K}_h(\boldsymbol{\theta}^{(1,0)}), \widetilde{K}_h(\boldsymbol{\theta}^{(0,1)}), \widetilde{K}_h(\boldsymbol{\theta}^{(1,1)}) \right\},$$
$$\widetilde{\boldsymbol{S}}_h(\boldsymbol{\theta},\omega) = \text{diag}\left\{ \widetilde{S}_h(\boldsymbol{\theta}^{(0,0)},\omega), \widetilde{S}_h(\boldsymbol{\theta}^{(1,0)},\omega), \widetilde{S}_h(\boldsymbol{\theta}^{(0,1)},\omega), \widetilde{S}_h(\boldsymbol{\theta}^{(1,1)},\omega) \right\},$$
$$\widetilde{\boldsymbol{R}}_h^H(\boldsymbol{\theta}) = \left(\widetilde{R}_h^H(\boldsymbol{\theta}^{(0,0)}), \widetilde{R}_h^H(\boldsymbol{\theta}^{(1,0)}), \widetilde{R}_h^H(\boldsymbol{\theta}^{(0,1)}), \widetilde{R}_h^H(\boldsymbol{\theta}^{(1,1)}) \right),$$
$$\widetilde{\boldsymbol{P}}_H^h(\boldsymbol{\theta}) = \left(\widetilde{P}_H^h(\boldsymbol{\theta}^{(0,0)}); \widetilde{P}_H^h(\boldsymbol{\theta}^{(1,0)}); \widetilde{P}_H^h(\boldsymbol{\theta}^{(0,1)}); \widetilde{P}_H^h(\boldsymbol{\theta}^{(1,1)}) \right),$$

in which $\text{diag}\{A_1, A_2, A_3, A_4\}$ refers to a block diagonal matrix with diagonal blocks A_1, A_2, A_3, and A_4. Furthermore, $\widetilde{K}_h$ is the symbol of the operator K_h as discussed in subsection 4.3 and $\widetilde{S}_h$ is the symbol of the additive Vanka-type smoother (we refer to [11, Sections 3.5 and 3.6] on how to compute this symbol). We refer to [18, Section 5.2], [11, Section 3.4], and [23] on how to compute $\widetilde{\boldsymbol{R}}_h^H$, the symbol of R_h^H, taking into account the different groups of DOFs. The symbol of P_H^h, $\widetilde{\boldsymbol{P}}_H^h$ follows from the symbol of R_h^H since $R_h^H = (P_H^h)^T$. Similarly, the symbol of the coarse-grid operator, $\widetilde{K}_H$, follows from the symbols of the grid-transfer operators and the fine-grid operator.

Given the symbol of E_h (4.30), the two-grid LFA asymptotic convergence factor, ρ_{asp}, is defined as [30, 35]

$$(4.31) \qquad\qquad \rho_{\text{asp}} = \sup_{\boldsymbol{\theta} \in T^{\text{low}}} \left\{ \rho\left(\widetilde{\boldsymbol{E}}_h(\boldsymbol{\theta},\omega)\right) \right\},$$

where $\rho(\widetilde{\boldsymbol{E}}_h(\boldsymbol{\theta},\omega))$ is the spectral radius of the matrix $\widetilde{\boldsymbol{E}}_h$. In section 5 we will approximate ρ_{asp} by sampling over a finite set of frequencies. In general, this approximation provides a sharp prediction of the two-grid performance.

5. Numerical Results. We will now use the LFA from section 4 to compare the efficiency of geometric multigrid (see section 3) for solving linear systems resulting from HDG, EDG, and CG discretizations of the Poisson problem. We furthermore compare the performance of the additive Vanka smoothers introduced in subsection 3.1 to the classical relaxation iterations of weighted pointwise Jacobi and Gauss–Seidel.
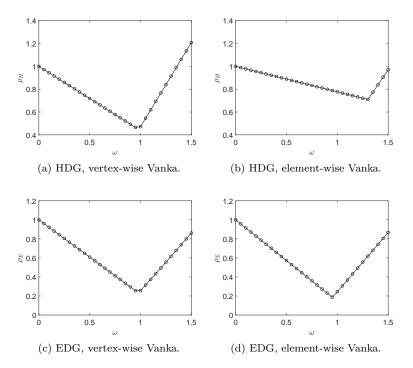
FIG. 5.1. *Variation of two-grid LFA convergence factor as a function of ω. Left column: the two-grid method using vertex-wise additive Vanka relaxation schemes. Right column: the two-grid method using element-wise additive Vanka relaxation schemes. The two-grid method is applied to HDG and EDG discretizations of the Laplacian with $k = 2$.*

For a fair comparison we use the ordering of the DOFs defined by the Vanka patches for all smoothers. In particular, the DOFs are ordered with N-type DOFs first, followed by X-type DOFs, Y-type DOFs, and C-type DOFs. Lexicographical ordering is used for each group of DOFs. In all our simulations we consider meshes with square elements and linear, quadratic, and cubic $(k = 1, 2, 3)$ polynomial approximations. In the HDG and EDG discretization (2.5) we furthermore set the penalty parameter to $\alpha = 6k^2$ [26].

5.1. LFA prediction of multigrid efficiency. The additive Vanka (3.2), weighted pointwise Jacobi and Gauss–Seidel relaxation schemes include a tunable parameter ω. By a brute-force approach we first determine the optimal value of ω that minimizes the two-grid convergence factor ρ_{asp} (see (4.31)) for each discretization and for each polynomial degree. For this we use 32×32 evenly distributed Fourier frequencies $\boldsymbol{\theta}$ in the Fourier domain $[-\frac{\pi}{2} + \epsilon, \frac{\pi}{2} - \epsilon]^2$ with $\epsilon = \pi/64$.

We first consider the case where we only use one pre-relaxation sweep and no post-relaxation sweeps in the two-grid method, i.e., $\nu_1 = 1$ and $\nu_2 = 0$. In Figure 5.1 we first plot the sensitivity of the two-grid LFA convergence factor with element- and vertex-wise additive Vanka relaxation schemes for the EDG and HDG discretization methods when $k = 2$. These plots indicate the importance of correctly choosing ω.

Next we present in Table 5.1 the computed optimal value of ω and the corresponding two-grid LFA convergence factor for the different discretization and relaxation methods. For the continuous Galerkin method with $k = 1$ and a pointwise Jacobi re-

TABLE 5.1

Two-grid LFA predictions with $\nu_1 = 1$ and $\nu_2 = 0$ of the spectral radii for CG, HDG, and EDG discretizations of the Laplacian. The number in brackets is the optimal value of ω that minimizes the spectral radius. Here ρ_C, ρ_E, ρ_H are the spectral radii of the two-grid method applied to a CG, EDG, and HDG discretization, respectively. We consider vertex-wise (VW), Lower-Triangular-Vertex-Wise (LTVW), element-wise (EW), and Lower-Triangular-Element-Wise (LTEW) additive Vanka type relaxation, pointwise Jacobi (JAC) relaxation and Gauss–Seidel (GS) relaxation. For each row, the best convergence factor among the smoothers that can be executed in parallel (i.e., excluding GS) is indicated in bold.

ρ	VW	EW	JAC	LTVW	LTEW	GS
			$k=1$			
$\rho_C(\rho_E)$	0.333(0.89)	**0.200**(0.90)	0.333(0.89)	0.333(0.89)	0.282(0.90)	0.261(1.02)
ρ_H	**0.403**(0.96)	0.466(1.14)	0.801(0.76)	0.609(1.12)	0.604(1.18)	0.394(1.30)
			$k=2$			
ρ_C	0.208(1.00)	0.282(0.84)	0.452(1.00)	0.362(1.02)	**0.188**(1.02)	0.167(1.06)
ρ_E	0.233(0.98)	**0.194**(0.96)	0.537(1.02)	0.423(1.08)	0.325(1.10)	0.246(1.10)
ρ_H	**0.449**(0.98)	0.710(1.30)	0.893(0.82)	0.802(1.18)	0.799(1.20)	0.628(1.50)
			$k=3$			
ρ_C	0.233(0.96)	**0.203**(0.94)	0.654(0.78)	0.368(1.08)	0.301(1.00)	0.233(1.10)
ρ_E	**0.287**(0.94)	0.332(1.10)	0.792(0.90)	0.598(1.20)	0.576(1.18)	0.470(1.30)
ρ_H	**0.476**(0.98)	0.794(1.32)	0.932(0.78)	0.862(1.22)	0.862(1.22)	0.745(1.50)

laxation method (which for CG with $k = 1$ is the same as a vertex-wise Vanka patch) it was proven that $\omega = 0.89$ is the optimal damping parameter [17, Lemma 4.1]. We therefore take $\omega = 0.89$ for this particular case and compute only the corresponding two-grid LFA convergence factor.

As expected, for $k = 1$, the spectral radius of the CG and EDG method are equal [7]. For $k = 2$ and $k = 3$ the LFA predicts that the performance of the two-grid method for EDG and CG are similar. We also note from Table 5.1 that the two-grid methods for EDG and CG outperform the two-grid method applied to an HDG discretization, no matter which relaxation scheme is used.

There is little difference between using vertex-wise and element-wise Vanka patches and Gauss–Seidel for the CG and EDG discretizations. For the HDG discretization the vertex-wise Vanka patch outperforms the element-wise Vanka patch. For all discretization methods LFA predicts that both the vertex-wise and element-wise Vanka patch approaches lead to smaller convergence factors than pointwise Jacobi.

We furthermore observe that although using a lower-triangular approximation to K_i in the additive Vanka relaxation scheme does not affect the two-grid LFA convergence factor too much for the CG and EDG discretizaion, the performance of the two-grid method for HDG significantly deteriorates with this approximation. We finally remark that, especially for the pointwise Jacobi smoother, the performance of the two-grid method slowly deteriorates with increasing k.

We next consider the performance of the two-grid method using different pre- and post relaxation sweeps. For ω we use the values from Table 5.1. In Table 5.2 we present the results predicted by LFA for the two-grid method using vertex-wise, element-wise and Lower-Triangular-Element-Wise additive Vanka type relaxation. We do not present the results here for pointwise Jacobi and Lower-Triangular-Vertex-Wise Vanka type relaxation because, for the same pre- and post relaxation sweeps, these are always worse than the previously mentioned relaxation schemes.

For all discretization and relaxation methods we observe that the convergence factor of the two-grid method is reduced when the number of pre- and post-relaxation sweeps are increased, however, this improvement is most notable for the CG and EDG

TABLE 5.2

Two-grid LFA predictions with different pre- and post relaxation sweeps of the spectral radii for CG, HDG, and EDG discretizations of the Laplacian. Here ρ_C, ρ_E, ρ_H are the spectral radii of the two-grid method applied to a CG, EDG, and HDG discretization, respectively. Furthermore $TG(\nu_1, \nu_2)$ denotes the two-grid method using ν_1 and ν_2 pre- and post relaxation sweeps.

k	ρ	TG(1,1)	TG(1,2)	TG(2,2)

Gauss–Seidel relaxation

k	ρ	TG(1,1)	TG(1,2)	TG(2,2)
1	$\rho_C(\rho_E)$	0.079	0.069	0.034
	ρ_H	0.238	0.108	0.058
2	ρ_C	0.071	0.042	0.028
	ρ_E	0.083	0.047	0.025
	ρ_H	0.387	0.241	0.157
3	ρ_C	0.095	0.044	0.023
	ρ_E	0.221	0.115	0.078
	ρ_H	0.555	0.410	0.306

Vertex-Wise Vanka relaxation

k	ρ	TG(1,1)	TG(1,2)	TG(2,2)
1	$\rho_C(\rho_E)$	0.112	0.078	0.061
	ρ_H	0.250	0.149	0.093
2	ρ_C	0.064	0.022	0.012
	ρ_E	0.096	0.042	0.034
	ρ_H	0.225	0.105	0.071
3	ρ_C	0.068	0.023	0.014
	ρ_E	0.122	0.057	0.042
	ρ_H	0.227	0.114	0.073

Element-Wise Vanka relaxation

k	ρ	TG(1,1)	TG(1,2)	TG(2,2)
1	$\rho_C(\rho_E)$	0.090	0.048	0.040
	ρ_H	0.342	0.193	0.138
2	ρ_C	0.079	0.022	0.009
	ρ_E	0.094	0.045	0.032
	ρ_H	0.518	0.360	0.274
3	ρ_C	0.104	0.032	0.017
	ρ_E	0.165	0.063	0.043
	ρ_H	0.631	0.501	0.398

Lower-Triangular-Element-Wise Vanka relaxation

k	ρ	TG(1,1)	TG(1,2)	TG(2,2)
1	$\rho_C(\rho_E)$	0.098	0.070	0.052
	ρ_H	0.456	0.284	0.226
2	ρ_C	0.065	0.043	0.030
	ρ_E	0.180	0.076	0.050
	ρ_H	0.672	0.529	0.456
3	ρ_C	0.117	0.057	0.032
	ρ_E	0.327	0.185	0.119
	ρ_H	0.743	0.640	0.551

TABLE 5.3

*Measured multigrid convergence factors. Notation: $\rho_{m,\alpha,\beta}$ is the measured asymptotic convergence factor of a two-grid ($\beta = TG$) or V-cyle multigrid ($\beta = MG$) method applied to a continuous Galerkin ($\alpha = C$), HDG ($\alpha = H$) or EDG ($\alpha = E$) discretization. The * indicates a case where the measured convergence factor according to (5.1) with tolerance 10^{-16} is not representative, since the ratio in (5.1) oscillates between consecutive iterates. In brackets we denote the value computed by $\rho_m = (\|d_h^{(j)}\|/\|d_h^{(0)}\|)^{1/j}$ which is approximately constant with iteration number asymptotically. For each row, the best convergence factor among the smoothers that can be executed in parallel (i.e., excluding GS) is indicated in bold.*

ρ	VW	EW	JAC	LTVW	LTEW	GS
			$k=1$			
$\rho_{m,C,TG}(\rho_{m,E,TG})$	0.332	**0.197**	0.332	0.332	0.252	0.242
$\rho_{m,C,MG}(\rho_{m,E,MG})$	0.332	**0.196**	0.332	0.332	0.255	0.177*(0.261)
$\rho_{m,H,TG}$	**0.396**	0.461	0.799	0.604	0.698	0.382
$\rho_{m,H,MG}$	**0.452**	0.606	0.800	0.680	0.694	0.587
			$k=2$			
$\rho_{m,C,TG}$	**0.200**	0.276	0.451	0.357	0.212	0.159
$\rho_{m,C,MG}$	0.211	0.276	0.450	0.357	**0.197**	0.162
$\rho_{m,E,TG}$	0.231	**0.192**	0.531	0.418	0.316	0.241
$\rho_{m,E,MG}$	**0.227**	0.269	0.530	0.418	0.319	0.290
$\rho_{m,H,TG}$	**0.433**	0.707	0.890	0.800	0.794	0.616
$\rho_{m,H,MG}$	**0.436**	0.707	0.890	0.800	0.792	0.626
			$k=3$			
$\rho_{m,C,TG}$	0.229	**0.198**	0.646	0.354	0.296	0.230
$\rho_{m,C,MG}$	0.225	**0.206**	0.653	0.359	0.314	0.254
$\rho_{m,E,TG}$	**0.281**	0.324	0.790	0.585	0.570	0.446
$\rho_{m,E,MG}$	**0.274**	0.324	0.789	0.608	0.591	0.466
$\rho_{m,H,TG}$	**0.472**	0.791	0.931	0.860	0.860	0.740
$\rho_{m,H,MG}$	**0.472**	0.790	0.931	0.859	0.859	0.747

discretizations. We furthermore observe that the performance of the two-grid method is always better when applied to the CG and EDG discretizations than when applied to the HDG discretization. We remark also that the two-grid method with Lower-Triangular-Element-Wise Vanka relaxation performs almost as well as the two-grid method with Element-Wise Vanka relaxation for the CG and EDG discretizations. This is particularly interesting for larger k since computing the inverse of the lower-triangular approximation to K_i in (3.1) is significantly cheaper than computing the inverse of K_i. Finally, we remark that always $(\rho(TG(1,0)))^{\nu_1+\nu_2} < \rho(TG(\nu_1,\nu_2))$. This implies that it is cheaper to apply $\nu_1 + \nu_2$ steps of the two-grid method with one pre-relaxation sweep and no post-relaxation sweeps than to apply the two-grid method with ν_1 pre-relaxation sweeps and ν_2 post-relaxation sweeps.

5.2. Measured multigrid convergence factors. In this section we verify the LFA predictions from subsection 5.1. For this we consider the Laplace problem on the unit square domain with homogeneous Dirichlet boundary conditions. We will solve HDG, EDG, and CG discretizations of this problem using geometric multigrid starting with a random initial guess with each component taken from a uniform distribution on $[0, 100]$. We will measure the asymptotic convergence behavior of the proposed two-grid method as well as its five-level V-cyle multigrid variant. For ω we use the values from Table 5.1. The finest mesh in our calculations consists of $64^2 = 4096$ elements and we use an LU-decomposition to solve the problem on the coarsest grid.

TABLE 5.4

Measured asymptotic convergence factors using different grid sizes. Notation: $\rho_{m,\alpha,\beta}$ is the measured asymptotic convergence factor of a two-grid ($\beta = TG$) or V-cyle multigrid ($\beta = MG$) method applied to a continuous Galerkin ($\alpha = C$), HDG ($\alpha = H$) or EDG ($\alpha = E$) discretization. In all cases we use element-wise Vanka relaxation for CG and EDG and vertex-wise relaxation for HDG.

Mesh	$\rho_{m,C,TG}$	$\rho_{m,C,MG}$	$\rho_{m,E,TG}$	$\rho_{m,E,MG}$	$\rho_{m,H,TG}$	$\rho_{m,H,MG}$
			$k=1$			
32^2	0.194	0.195	0.194	0.195	0.396	0.429
64^2	0.197	0.196	0.197	0.196	0.396	0.452
128^2	0.196	0.196	0.196	0.196	0.396	0.471
256^2	0.197	0.197	0.197	0.197	0.395	0.477
			$k=2$			
32^2	0.276	0.277	0.194	0.255	0.432	0.436
64^2	0.276	0.276	0.192	0.269	0.433	0.436
128^2	0.277	0.277	0.191	0.270	0.434	0.437
256^2	0.278	0.278	0.191	0.270	0.434	0.437
			$k=3$			
32^2	0.198	0.207	0.324	0.323	0.471	0.470
64^2	0.198	0.206	0.324	0.324	0.472	0.472
128^2	0.199	0.206	0.324	0.324	0.472	0.472
256^2	0.206	0.206	0.324	0.324	0.472	0.472

The measured asymptotic convergence factor is given by

$$
(5.1) \qquad \rho_m = \frac{\|d_h^{(j)}\|_2}{\|d_h^{(j-1)}\|_2},
$$

where $d_h^{(j)} = f_h - K_h \bar{\boldsymbol{u}}_h^{(j)}$, $\bar{\boldsymbol{u}}_h^{(j)}$ is the approximation to the solution of (2.11) at the jth multigrid iteration, and j is the smallest integer such that $\|d_h^{(j)}\|_2 < 10^{-16}$.

Remark 5.1. Other approaches to measure the asymptotic convergence factor are to define ρ_m as $\rho_m = (\|d_h^{(j)}\| / \|d_h^{(0)}\|)^{1/j}$ or $\rho_m = (\|\bar{\boldsymbol{u}}_h^{(j)}\| / \|\bar{\boldsymbol{u}}_h^{(0)}\|)^{1/j}$. For our problem, the results obtained using these measures are almost the same as when using (5.1).

In Table 5.3 we present the measured asymptotic convergence factors for the case where we use one pre-relaxation sweep and no post-relaxation sweeps, i.e., $\nu_1 = 1$ and $\nu_2 = 0$. We observe that the measured asymptotic convergence factors match very well with the two-grid LFA convergence factors in Table 5.1, verifying our analysis. In particular, these results confirm that performance of geometric multigrid applied to an EDG discretization is similarly effective in terms of convergence factors and scalability as for geometric multigrid applied to a continuous Galerkin discretization, and that this performance is always substantially better than when applied to an HDG discretization. The results in Table 5.3 show that, among the smoothers that can be executed in parallel, the Vanka-type smoothers may require substantially less multigrid iterations than the Jacobi smoother, especially as the order of the discretization increases.

We remark that we also measured the asymptotic convergence factor for W- and F-cycle multigrid, but compared to V-cycle multigrid there was only very minor improvement. We furthermore remark that the conclusions for the $(\nu_1, \nu_2) = (1, 0)$ case hold also for other (ν_1, ν_2) combinations. We therefore do not present these results here.

Finally, in Table 5.4 we show that the measured asymptotic convergence factors of the two-grid and V-cyle multigrid methods (with $(\nu_1, \nu_2) = (1, 0)$) are independent of the mesh size h. We present the results only for the case where we use element-wise Vanka relaxation for CG and EDG, and vertex-wise Vanka relaxation for HDG. We see that the measured two-grid convergence factors match well with the two-grid LFA predictions from Table 5.1. The measured convergence factors of V-cycle multigrid methods for CG are the same as the two-grid LFA predictions. For EDG with $k = 2$ and HDG with $k = 1$, the measured V-cycle convergence factors are a little worse than the measured two-grid convergence factors. This is as expected, since in a V-cycle, we use an inexact solver (multigrid) for the coarse problem, instead of the exact coarse solver of the two-grid method. All in all, the two-grid and V-cycle multigrid methods offer efficient performance. We remark that for $k = 3$, the values $\rho_{m,\alpha,TG}$ are measured using a three-level V-cycle, since in the two-grid method the LU decomposition for the coarse problem runs out of memory on the computer we used.

6. Conclusions. We presented a geometric multigrid method with Jacobi and additive Vanka relaxation for continuous Galerkin, EDG and HDG discretizations of the Poisson problem. We used local Fourier analysis to predict the efficiency of the multigrid method and confirmed what we have observed in previous work [25], namely that (algebraic) multigrid performance applied to an EDG discretization outperforms multigrid applied to an HDG discretization. We therefore conclude that although EDG does not have the super-convergence properties of an HDG discretization [7], EDG methods with suitable iterative methods are competitive alternatives to HDG discretizations. More generally, our work represents the first analysis of geometric multigrid convergence for high-order EDG and HDG discretizations in two dimensions, demonstrating fast convergence, in particular for EDG.

Appendix A. Stencil example for HDG with $k = 1$.
We present here an example of the stencils (4.8) for the HDG method with $k = 1$. Using (4.6) (or (4.5)) and (4.8) we can write

$$(A.1) \qquad K_h = \begin{bmatrix} [s_{\boldsymbol{\kappa}}]_{X_1 X_1} & [s_{\boldsymbol{\kappa}}]_{X_1 X_2} & [s_{\boldsymbol{\kappa}}]_{X_1 Y_1} & [s_{\boldsymbol{\kappa}}]_{X_1 Y_2} \\ [s_{\boldsymbol{\kappa}}]_{X_2 X_1} & [s_{\boldsymbol{\kappa}}]_{X_2 X_2} & [s_{\boldsymbol{\kappa}}]_{X_2 Y_1} & [s_{\boldsymbol{\kappa}}]_{X_2 Y_2} \\ [s_{\boldsymbol{\kappa}}]_{Y_1 X_1} & [s_{\boldsymbol{\kappa}}]_{Y_1 X_2} & [s_{\boldsymbol{\kappa}}]_{Y_1 Y_1} & [s_{\boldsymbol{\kappa}}]_{Y_1 Y_2} \\ [s_{\boldsymbol{\kappa}}]_{Y_2 X_1} & [s_{\boldsymbol{\kappa}}]_{Y_2 X_2} & [s_{\boldsymbol{\kappa}}]_{Y_2 Y_1} & [s_{\boldsymbol{\kappa}}]_{Y_2 Y_2} \end{bmatrix}.$$

Since the DOFs in HDG are only of type X and Y the different stencils in (A.1) are only of type 1 and 4 (see subsection 4.2 for a definition of the four different stencil types). Using $\alpha = 6k^2$ these stencils are given by

$$[s_{\boldsymbol{\kappa}}]_{X_1 X_1} = \begin{bmatrix} -1/24 \\ 9/4\odot \\ -1/24 \end{bmatrix}, \qquad\qquad [s_{\boldsymbol{\kappa}}]_{X_1 X_2} = \begin{bmatrix} -1/24 \\ 11/12\odot \\ -1/24 \end{bmatrix},$$

$$[s_{\boldsymbol{\kappa}}]_{X_1 Y_1} = \begin{bmatrix} -19/24 & & -7/24 \\ & \odot & \\ -7/24 & & -1/8 \end{bmatrix}, \qquad [s_{\boldsymbol{\kappa}}]_{X_1 Y_2} = \begin{bmatrix} -7/24 & & -1/8 \\ & \odot & \\ -19/24 & & -7/24 \end{bmatrix},$$

$$[s_{\boldsymbol{\kappa}}]_{X_2 X_1} = \begin{bmatrix} -1/24 \\ 11/12 \odot \\ -1/24 \end{bmatrix}, \qquad [s_{\boldsymbol{\kappa}}]_{X_2 X_2} = \begin{bmatrix} -1/24 \\ 9/4 \odot \\ -1/24 \end{bmatrix},$$

$$[s_{\boldsymbol{\kappa}}]_{X_2 Y_1} = \begin{bmatrix} -7/24 & & -19/24 \\ & \odot & \\ -1/8 & & -7/24 \end{bmatrix}, \qquad [s_{\boldsymbol{\kappa}}]_{X_2 Y_2} = \begin{bmatrix} -1/8 & & -7/24 \\ & \odot & \\ -7/24 & & -19/24 \end{bmatrix},$$

$$[s_{\boldsymbol{\kappa}}]_{Y_1 X_1} = \begin{bmatrix} -1/8 & & -7/24 \\ & \odot & \\ -7/24 & & -19/24 \end{bmatrix}, \qquad [s_{\boldsymbol{\kappa}}]_{Y_1 X_2} = \begin{bmatrix} -7/24 & & -1/8 \\ & \odot & \\ -19/24 & & -7/24 \end{bmatrix},$$

$$[s_{\boldsymbol{\kappa}}]_{Y_1 Y_1} = \begin{bmatrix} -1/24 & 9/4 \odot & -1/24 \end{bmatrix}, \qquad [s_{\boldsymbol{\kappa}}]_{Y_1 Y_2} = \begin{bmatrix} -1/24 & 11/12 \odot & -1/24 \end{bmatrix},$$

$$[s_{\boldsymbol{\kappa}}]_{Y_2 X_1} = \begin{bmatrix} -7/24 & & -19/24 \\ & \odot & \\ -1/8 & & -7/24 \end{bmatrix}, \qquad [s_{\boldsymbol{\kappa}}]_{Y_2 X_2} = \begin{bmatrix} -19/24 & & -7/24 \\ & \odot & \\ -7/24 & & -1/8 \end{bmatrix},$$

$$[s_{\boldsymbol{\kappa}}]_{Y_2 Y_1} = \begin{bmatrix} -1/24 & 9/4 \odot & -1/24 \end{bmatrix}, \qquad [s_{\boldsymbol{\kappa}}]_{Y_2 Y_2} = \begin{bmatrix} -1/24 & 11/12 \odot & -1/24 \end{bmatrix}.$$

REFERENCES

[1] J. H. Adler, T. R. Benson, and S. P. MacLachlan, *Preconditioning a mass-conserving discontinuous Galerkin discretization of the Stokes equations*, Numer. Linear Algebra Appl., 24 (2017), pp. e2047, 23, https://doi.org/10.1002/nla.2047.

[2] T. Boonen, J. Van lent, and S. Vandewalle, *Local Fourier analysis of multigrid for the curl-curl equation*, SIAM J. Sci. Comput., 30 (2008), pp. 1730–1755, https://doi.org/10.1137/070679119.

[3] A. Brandt, *Multi-level adaptive solutions to boundary-value problems*, Math. Comp., 31 (1977), pp. 333–390, https://doi.org/10.2307/2006422.

[4] H. Chen, P. Lu, and X. Xu, *A robust multilevel method for hybridizable discontinuous Galerkin method for the Helmholtz equation*, J. Comput. Phys., 264 (2014), pp. 133–151, https://doi.org/10.1016/j.jcp.2014.01.042.

[5] B. Cockburn, O. Dubois, J. Gopalakrishnan, and S. Tan, *Multigrid for an HDG method*, IMA J. Numer. Anal., 34 (2014), pp. 1386–1425, https://doi.org/10.1093/imanum/drt024.

[6] B. Cockburn, J. Gopalakrishnan, and R. Lazarov, *Unified hybridization of discontinuous Galerkin, mixed, and continuous Galerkin methods for second order elliptic problems*, SIAM J. Numer. Anal., 47 (2009), pp. 1319–1365, https://doi.org/10.1137/070706616.

[7] B. Cockburn, J. Guzmán, S. C. Soon, and H. K. Stolarski, *An analysis of the embedded discontinuous Galerkin method for second-order elliptic problems*, SIAM J. Numer. Anal., 47 (2009), pp. 2686–2707, https://doi.org/10.1137/080726914.

[8] H. De Sterck, S. Friedhoff, A. J. Howse, and S. P. MacLachlan, *Convergence analysis for parallel-in-time solution of hyperbolic systems*, Numer. Linear Algebra Appl., 27 (2020), p. e2271, https://doi.org/10.1002/nla.2271.

[9] V. Dobrev, T. Kolev, C. S. Lee, V. Tomov, and P. S. Vassilevski, *Algebraic hybridization and static condensation with application to scalable H(div) preconditioning*, SIAM J. Sci. Comput., 41 (2019), pp. B425–B447, https://doi.org/10.1137/17M1132562.

[10] M. S. Fabien, M. G. Knepley, R. T. Mills, and B. M. Rivière, *Manycore parallel computing for a hybridizable discontinuous Galerkin nested multigrid method*, SIAM J. Sci. Comput., 41 (2019), pp. C73–C96, https://doi.org/10.1137/17M1128903.

[11] P. E. Farrell, Y. He, and S. P. MacLachlan, *A local Fourier analysis of additive Vanka relaxation for the Stokes equations*, Numer. Linear Algebra Appl., (2020). To appear.

[12] K. J. Fidkowski, T. A. Oliver, J. Lu, and D. L. Darmofal, *p-multigrid solution of high-order discontinuous Galerkin discretizations of the compressible Navier–Stokes equations*, J. Comput. Phys., 207 (2005), pp. 92–113, https://doi.org/10.1016/j.jcp.2005.01.005.

[13] A. Frommer and D. B. Szyld, *Weighted max norms, splittings, and overlapping additive Schwarz iterations*, Numer. Math., 83 (1999), pp. 259–278, https://doi.org/10.1007/s002110050449.

[14] J. Gopalakrishnan and G. Kanschat, *A multilevel discontinuous Galerkin method*, Numer. Math., 95 (2003), pp. 527–550, https://doi.org/10.1007/s002110200392.

[15] J. Gopalakrishnan and S. Tan, *A convergent multigrid cycle for the hybridized mixed method*, Numer. Linear Algebra Appl., 16 (2009), pp. 689–714, https://doi.org/10.1002/nla.636.

[16] S. Güzey, B. Cockburn, and H. K. Stolarski, *The embedded discontinuous Galerkin methods: Application to linear shells problems*, Int. J. Numer. Methods Engrg., 70 (2007), pp. 757–790, https://doi.org/10.1002/nme.1893.

[17] Y. He and S. P. MacLachlan, *Local Fourier analysis for mixed finite-element methods for the Stokes equations*, J. Comput. Appl. Math., 357 (2019), pp. 161–183, https://doi.org/10.1016/j.cam.2019.01.029.

[18] Y. He and S. P. MacLachlan, *Two-level Fourier analysis of multigrid for higher-order finite-element discretizations of the Laplacian*, Numer. Linear Algebra Appl., 27 (2020), pp. e2285, 26, https://doi.org/10.1002/nla.2285.

[19] P. W. Hemker, W. Hoffmann, and M. H. van Raalte, *Two-level Fourier analysis of a multigrid approach for discontinuous Galerkin discretization*, SIAM J. Sci. Comput., 25 (2003), pp. 1018–1041, https://doi.org/10.1137/S1064827502405100.

[20] P. W. Hemker and M. H. van Raalte, *Fourier two-level analysis for higher dimensional discontinuous Galerkin discretisation*, Comput. Vis. Sci., 7 (2004), pp. 159–172, https://doi.org/10.1007/s00791-004-0136-1.

[21] R. M. Kirby, S. J. Sherwin, and B. Cockburn, *To CG or to HDG: a comparitive study*, J. Sci. Comput., 51 (2012), pp. 183–212, https://doi.org/10.1007/s10915-011-9501-7.

[22] M. Kronbichler and W. A. Wall, *A performance comparison of continuous and discontinuous Galerkin methods with fast multigrid solvers*, SIAM J. Sci. Comput., 40 (2018), pp. A3423–A3448, https://doi.org/10.1137/16M110455X.

[23] S. P. MacLachlan and C. W. Oosterlee, *Local Fourier analysis for multigrid with overlapping smoothers applied to systems of PDEs*, Numer. Linear Algebra Appl., 18 (2011), pp. 751–774, https://doi.org/10.1002/nla.762.

[24] S. Rhebergen and G. N. Wells, *Preconditioning of a hybridized discontinuous galerkin finite element method for the Stokes equations*, J. Sci. Comput., 77 (2018), pp. 1936–1952, https://doi.org/10.1007/s10915-018-0760-4.

[25] S. Rhebergen and G. N. Wells, *An embedded-hybridized discontinuous Galerkin finite element method for the Stokes equations*, Comput. Methods Appl. Mech. Engrg., 358 (2020), pp. 112619, 1–18, https://doi.org/10.1016/j.cma.2019.112619.

[26] B. Rivière, *Discontinuous Galerkin Methods for Solving Elliptic and Parabolic Equations*, vol. 35 of Frontiers in Applied Mathematics, Society for Industrial and Applied Mathematics, Philadelphia, 2008.

[27] C. Rodrigo, F. Sanz, F. J. Gaspar, and F. J. Lisbona, *Local Fourier analysis for edge-based discretizations on triangular grids*, Numer. Math. Theor. Meth. Appl., 8 (2015), pp. 78–96, https://doi.org/10.4208/nmtma.2015.w07si.

[28] Y. Saad, *Iterative methods for sparse linear systems*, Society for Industrial and Applied Mathematics, Philadelphia, PA, second ed., 2003, https://doi.org/10.1137/1.9780898718003.

[29] R. S. Sampath and G. Biros, *A parallel geometric multigrid method for finite elements on octree meshes*, SIAM J. Sci. Comput., 32 (2010), pp. 1361–1392, https://doi.org/10.1137/090747774.

[30] U. Trottenberg, C. W. Oosterlee, and A. Schüller, *Multigrid*, Academic Press, Inc., San Diego, CA, 2001.

[31] J. J. W. van der Vegt and S. Rhebergen, *hp-Multigrid as smoother algorithm for higher order discontinuous Galerkin discretizations of advection dominated flows. Part I. Multilevel analysis*, J. Comput. Phys., 231 (2012), pp. 7537–7563, https://doi.org/10.1016/j.jcp.2012.05.038.

[32] J. J. W. van der Vegt and S. Rhebergen, *hp-Multigrid as smoother algorithm for higher order discontinuous Galerkin discretizations of advection dominated flows. Part II. Optimization of the Runge–Kutta smoother*, J. Comput. Phys., 231 (2012), pp. 7563–7583, https://doi.org/10.1016/j.jcp.2012.05.037.

[33] M. H. van Raalte and P. W. Hemker, *Two-level multigrid analysis for the convection-diffusion equation discretized by a discontinuous Galerkin method*, Numer. Linear Algebra Appl., 12 (2005), pp. 563–584, https://doi.org/10.1002/nla.441.

[34] G. N. Wells, *Analysis of an interface stabilized finite element method: the advection-diffusion-reaction equation*, SIAM J. Numer. Anal., 49 (2011), pp. 87–109, https://doi.org/10.1137/090775464.

[35] R. Wienands and W. Joppich, *Practical Fourier analysis for multigrid methods*, vol. 4 of Numerical Insights, Chapman & Hall/CRC, Boca Raton, FL, 2005.

[36] T. Wildey, S. Muralikrishnan, and T. Bui-Thanh, *Unified geometric multigrid algorithm for hybridized high-order finite element methods*, SIAM J. Sci. Comput., 41 (2019), pp. S172–S195, https://doi.org/10.1137/18M1193505.

[37] S. Yakovlev, D. Moxey, R. M. Kirby, and S. J. Sherwin, *To CG or to HDG: a comparitive study in 3D*, J. Sci. Comput., 67 (2016), pp. 192–220, https://doi.org/10.1007/s10915-015-0076-6.